Characteristics of Precipitation Particle Distribution in Convective Cells around Okinawa Island during the Baiu Period

OUE, Mariko

Characteristics of precipitation particle distribution in convective cells around Okinawa Island during the Baiu period

(梅雨期沖縄域における対流セル内の降水粒子分布特性)

OUE, Mariko

(尾上　万里子)

A dissertation for the degree of Doctor of Science

Department of Earth and Environmental Sciences,

Graduate School of Environmental Studies, Nagoya University

(名古屋大学大学院環境学研究科地球環境科学専攻学位論文 博士 (理学))

Abstract

Convective cells with low echo-top heights are commonly observed in the humid environments typical of the Baiu season around Okinawa Island. Representative convective cells with low echo-top heights include convective cells in the stratiform and convective rain zones accompanying a precipitation system, as well as isolated convective cells. In recent years, a few studies have reported the convective cells in stratiform rain zones as one of the characteristic convective cell in the humid environments. The precipitation particle distribution and precipitation formation process for these convective cells have not been revealed. The purpose of this study is to clarify distributions of precipitation particles in convective cells, with low echo-top height, developing in a humid environment. We analyzed polarimetric radar variables and ground-based raindrop size distribution (DSD) and estimated DSD parameters for convective cells with low echo-top heights around Okinawa Island during the Baiu period of 2006, using a C-band polarimetric radar and a disdrometer.

First, precipitation particle distribution was analyzed for a convective cell in a stratiform rain zone and a convective cell in a convective rain zone, with 30-dBZ echo top less than 6 km above sea level (ASL), associated with a Baiu frontal rainband. The two convective cells were observed by range height indicators (RHIs) of the radar when they passed over the disdrometer. For the convective cell in the stratiform rain zone, analyses of polarimetric radar variables, differential reflectivity (Z_{DR}) and correlation coefficient (ρ_{hv}), in an RHI showed that small raindrops predominated in the convective cells below 0°C altitude; Z_{DR} was smaller than 1.5 dB, and ρ_{hv} was greater than 0.98, with large radar reflectivity (Z_{h}) below about 3 km ASL. The ground-based DSD showed high num-

ber densities of smaller raindrops (1−2 mm in diameter), with few raindrops exceeding 3 mm in diameter. On the other hand, for the convective cells in the convective rain zone, large raindrops contributed to the large radar reflectivity; $Z_{\rm DR}$ greater than 1.5 dB and $\rho_{\rm hv}$ smaller than 0.98 predominated, with large $Z_{\rm h}$ greater than 40 dBZ in an RHI below 3 km ASL. The peak of $Z_{\rm DR}$ value were shown particularly below 2 km ASL. The ground-based DSD showed large numbers of raindrops exceeding 3 mm in diameter.

To investigated variations in DSD characteristics with time and height, median volume diameter (D_0) and normalized intercept parameter (N_w) were estimated for cell lifetime using plan position indicator (PPI) volume scan data. For detailed analyses of time variations, we selected three convective calls, with 30-dBZ echo-top heights less than 6 km ASL, developing over the sea and observed by PPI volume scanning for their lifetimes (a convective cell in the stratiform rain zone of the Baiu frontal rainband, a convective cell in the convective rain zone of the rainband, and an isolated convective cell developing to the south of the Baiu front). To examine DSD characteristics contributing to $Z_{\rm h}$, the estimated DSD parameters from range bin data of PPIs in a rain region were averaged every 5 dB in $Z_{\rm h}$. For the convective cell in the stratiform rain zone in the mature stage, the estimated D_0 was approximately 1.5 mm with $Z_{\rm h}$ of 45−50 dBZ and did not reach 2 mm even when $Z_{\rm h}$ approached a large value of 50 dBZ; the estimated N_w ranged from 32000 to 100000 mm^{-1} m^{-3}. This indicates that a high number-concentration of small raindrops contributed to large $Z_{\rm h}$ for the convective cell in the stratiform rain zone. For the convective cell in the convective rain zone in the mature stage, the estimated D_0 was approximately 2 mm with $Z_{\rm h}$ of 40−45 dBZ; the estimated N_w ranged from 1000 to 10000 mm^{-1} m^{-3}. This indicates that large raindrops contributed to large $Z_{\rm h}$ for the convective cell in the convective rain zone. For the isolated convective cell in the mature stage,

D_0 was estimated to be approximately 2 mm with $Z_{\rm h}$ of 40−50 dBZ; the estimated N_w ranged from 1000 to 10000 mm^{-1} m^{-3}. This indicates that large raindrops contributed to large $Z_{\rm h}$ for the isolated convective cell. Analyses of variations in the estimated D_0 and N_w within cell lifetimes indicated that the D_0 values for a given $Z_{\rm h}$ for the convective cell in the convective rain zone and for the isolated convective cell were larger than those for the convective cell in the stratiform rain zone at any given time. The N_w values for the convective cell in the stratiform rain zone were larger than those for the other two cases at any given time.

From variations of vertical structure of the radar-estimated D_0 and N_w with convective lifetime, we suggested conceivable formation process of raindrops in each of the convective cells. For the convective cell in the stratiform rain zone, a high number-concentration of small raindrops contributed to the increase in $Z_{\rm h}$. In the convective cell in the convective rain zone and the isolated convective cell, large raindrops contributed to the increase in $Z_{\rm h}$ and raindrop coalescence processes were predominant at altitudes below 2 km ASL. The significance of these D_0 and N_w characteristics was confirmed for 25 cells in the stratiform rain zone, for 28 cells in the convective rain zone, for 14 isolated convective cells from the estimated D_0 and N_w for a given $Z_{\rm h}$ using PPI volume scan data.

This study characterized precipitation particle distribution for three types of convective cell, with low echo-top heights, representing the humid environment of Okinawa Island during the Baiu period. In particular, the precipitation particle distribution for convective cells in the stratiform rain zone, which differ markedly from convective cells in the convective rain zone and isolated convective cells, were newly characterized.

Contents

1 Introduction

1.1 Background

Convective cells produce large amounts of precipitation in short time periods. They have typical horizontal scales of less than 20 km (meso-γ scale) and are the principal components of precipitation systems that sometimes provide heavy rainfall during the rainy, humid Baiu period from June to July in Japan (Ninomiya et al., 1988; Ninomiya and Akiyama, 1992). As hydrometeor growth, phase transition, and decay by evaporation occur in convective cells, microphysical processes affect the spatial and size distributions of precipitation particles such as raindrop size distribution (DSD). Clarification of the microphysical structure of convective cells is important for understanding the microphysics and precipitation formation in humid regions during the Baiu period.

A number of studies of heavy rainfall formation over the East Asian humid region have examined convective cells. Several studies of them have suggested that convective cells in humid environments during the Baiu period show low echo-top heights in radar data. Zhang et al. (2006) reported that convection of medium depth with low 15-dBZ echo-top height below 8 km characterized convection around the Meiyu (Baiu) front in China. Kato et al. (2007) reported a level of neutral buoyancy at mid-altitude ($\sim$ 700 hPa), suggesting the existence of cumulonimbi with cloud tops lower than several kilometers in the Baiu frontal zone. Around Okinawa Island which is located in the East China Sea, particularly humid conditions occur during the Baiu period. Several researchers have reported an existence of convective cells with relatively low echo-top heights in the humid environment (Shusse et al., 2009). Shinoda et al. (2007) demonstrated that convective cells ($\geq$ 30 dBZ) with low echo-top heights less than 1 km above the environmental 0°C

level accounted for approximately 80% of convective cells observed by a Doppler radar in the Okinawa region during the Baiu period.

In the Okinawa region, radar observations often show not only convective cells existing in the convective portion of a precipitation system associated with the Baiu front (called a Baiu frontal rainband) but also convective cells existing in the stratiform rain region. In recent years, a few studies have identified the convective cells in stratiform rain zones as one of the characteristic convective cell types in humid environments. Bringi et al. (2006) performed quantitative precipitation estimation for convective cells embedded in the stratiform rain area of a Baiu event around Okinawa Island, using a polarimetric radar. Shusse et al. (2009) pointed out that convective cells embedded in the stratiform rain area are an ordinary occurrence in a Baiu event around Okinawa Island. The convective cells with low echo-top heights referred to in previous papers, namely convective cells in the stratiform rain zone (A in Fig. 1), convective cells in the convective rain zone (B in Fig. 1), and isolated convective cells (C in Fig. 1) are representative of those found around Okinawa Island during the Baiu. These convective cells sometimes have intense radar reflectivity and provide heavy rainfall, even though the echo-top heights are not much higher than 0°C altitude. Akaeda et al. (1991) explained the evolution of convective systems over Okinawa Island by the internal flow of the system and the propagation of convective cells making up the system. However, previous studies did not reveal the microphysical structures (spatial and size distributions of precipitation particles and DSD) of convective cells with low echo-top heights, and thus their microphysics and precipitation formation processes remain unclear. In particular, convective cells the embedded in the stratiform rain zone is an emerging type. To understand how and why these convective cells have large radar reflectivity and provide intense rainfall, despite having low

echo-top height, the raindrop size distribution (DSD) and microphysics presented as DSD are worth investigating.

The DSDs in convective cells are fundamental for understanding the microphysics of precipitation in convective cells. Clarification of DSD variation over the lifetimes of convective cells and the spatial distribution of DSD in convective cells is particularly important for understanding DSD characteristics and microphysics (Atlas and Ulbrich, 2000). The DSDs of rain events have been studied for several decades, more vigorously in recent years. Many of these studies have examined differences in DSD between convective rain and stratiform rain, and/or between continental storms and maritime storms, by analyzing ground-based DSDs (e.g., Tokay and Short, 1996; Maki et al., 2001; Atlas and Ulbrich, 2006; Kozu et al., 2006; Ulbrich and Atlas, 2007; Bringi et al., 2009). These studies analysed ground-based DSD measured by disdrometers, which measure the number and diameter of raindrops striking the ground and are major instruments for DSD on the ground.

Polarimetric radars have been used to investigate the spatial distributions of raindrop size especially for severe storms (e.g., Yuter and Houze Jr., 1995; Wang and Carey, 2005) based on features of polarimetric radar variables. This type of radar transmits and receives horizontally and vertically polarized radio waves, and measures the signal returns at horizontal (h) and vertical (v) polarizations. From the signal returns, reflectivity at horizontal polarization (Z_{h}) and other polarimetric variables such as differential reflectivity (Z_{DR}) and the correlation coefficient (ρ_{hv}) can be obtained. Polarimetric radar variables provide information about the categories and sizes of precipitation particles predominating within the radar resolution volume. The spatial and size distributions of precipitation particles are inseparably connected to radar reflectivity, which varies with

the size distributions and type (e.g., rain, snow, graupel) of precipitation particles. By analyzing a combination of radar reflectivity (Z_{h}) and other polarimetric parameters, we can infer the microphysical structures of heavy rainfalls represented by large radar reflectivity. Estimation of DSD parameters based on the polarimetric radar variables is available (Gorgucci et al., 2002; Bringi et al., 2003).

Recent studies have retrieved DSD parameters from polarimetric radar variables for convective precipitation systems developing in various types of environments, with the goal of quantitative estimation of rainfall intensity. Bringi et al. (2003) characterized DSD parameters retrieved from polarimetric radar measurements and those derived from disdrometer measurements for convective rain in different climate regimes. stratiform precipitation occurring in Darwin, Australia. Several researchers have used polarimetric radar analysis techniques to investigate precipitation mechanisms over subtropical humid regions of East Asia in recent years. Wang and Carey (2005) investigated the development and structure of a squall-line system over the South China Sea. Using polarimetric radar, they revealed the microphysical structures of convective cells accompanying the squall line that developed above 10 km in altitude. However, there are few studies which examined spatial distributions of DSD parameters using polarimetric radar measurements for convective cells with low echo-top heights.

Shusse et al. (2009) analyzed polarimetric radar variables and identified a convective cell embedded in a stratiform rainfall area around Okinawa Island in the Baiu period; the characteristics of polarimetric radar variables for the embedded convective cell were similar to those for stratiform rain and suggested that raindrops below the 2 km altitude of the embedded convective cell were smaller than those of an isolated convective cell. Only a few studies of polarimetric radar and DSD have examined convective cells with relatively

low echo-top heights around Okinawa Island during the Baiu period, and thus their microphysics and precipitation formation process remain unclear. Particularly, convective cells accompanying the Baiu frontal rainband, convective cells in the stratiform rain zone and convective cells in the convective rain zone, have not been attracted. To understand the microphysics and precipitation formation in convective cells that develop in humid environments, we must clarify the microphysical structure, spatial and size distributions of precipitation particles, in these convective cells with low echo-top heights and large radar reflectivity. The temporal variations of DSD within lifetime of convective cells is more helpful to understand the microphysics and precipitation formation of the convective cells with low echo-top heights (Atlas and Ulbrich, 2000; Hashimoto and Harimaya, 2005).

Thus, our objective was to clarify the spatial and size distributions of precipitation particles and DSD parameters causing large radar reflectivity in convective cells with low echo-top heights developing around Okinawa Island during the Baiu period. On Okinawa Island, the National Institute of Information and Communications Technology (NICT) operates a C-band (5.3 GHz) polarimetric radar named the CRL Okinawa bistatic polarimetric radar (COBRA) since 2002 and also operates ground-based instruments including disdrometers. Under an agreement between Nagoya University's Hydrospheric Atmospheric Research Center and the NICT, the polarimetric radar was specially operated for intensive observations of precipitation systems in a humid environment during the 2006 Baiu period, when the COBRA was operational and provided useful data of various parameters. We analyze polarimetric radar variables and ground-based raindrop size distribution (DSD) and estimated DSD parameters for convective cells with low echo-top heights around Okinawa Island during the Baiu period of 2006 using the C-band polarimetric radar and a disdrometer. From the results, we discuss microphysics and

precipitation formation in the convective cells developing in the humid environment.

First, this paper describes polarimetric radar variables for the two types of convective cells with large radar reflectivity and relatively low echo-top heights: one type of convective cells existed in the stratiform rain zone, and the other was convective cells existed in the convective zone of the precipitation system. These types of convective cells have not been focused for the microphysical structure, although they are commonly observed in humid environments. Actually, around Okinawa Island in the observation period during the Baiu of 2006, convective cells with low echo-top heights were also observed in convective and stratiform rain zones of precipitation systems by the polarimetric radar. We demonstrate the spatial distributions of precipitation particles in these convective cells using polarimetric radar and disdrometer analyses. Secondly, on the basis of the polarimetric radar variables, we clarify the DSD parameters for one typical case selected from each of three types of convective cells around Okinawa Island: a convective cell in the convective rain zone, a convective cell in the stratiform rain zone, and an isolated convective cell. From the estimated DSD parameters, the conceivable microphysics for each of the convective cells is discussed. Additionally, we discuss characteristics of DSD for convective cells with low echo-top heights in the Baiu period by comparing the estimated DSD parameters with those for other environments described in previous studies. To exhibit the DSD characteristics in detail for these convective cells, clarification of polarimetric radar variables for the convective cells is necessary. The polarimetric radar variables and DSD parameters, which are effective for understanding microphysics and precipitation formation and used in this study, are expressed in section 1.2 and 1.3, respectively.

1.2 Polarimetric radar variables

A polarimetric radar analysis of polarimetric radar variables (radar reflectivity at horizontal polarization Z_{h}, Z_{DR}, and ρ_{hv}) is useful to reveal the spatial distribution of precipitation particles. Many researchers have used these variables to characterize precipitation particles (e.g., Bringi et al., 1991; Yuter and Houze Jr., 1995; Atlas and Williams, 2003).

Generally, the Rayleigh-Gans limit is a good approximation in a rain region. In the Rayleigh-Gans limit, the radar reflectivity factor (Z) in units of $\mathrm{mm^6 m^{-3}}$ for a rain region is defined as

$$Z = \int_{D_{min}}^{D_{max}} D^6 N(D) dD, \tag{1}$$

where D is the diameter of raindrops in mm, and $N(D)dD$ is the number of spheres per cubic meter in the diameter interval (D, $D + dD$).

The differential reflectivity, Z_{DR}, in the unit of dB is defined as

$$Z_{\mathrm{DR}} = 10 \log_{10} \frac{|Z_{\mathrm{h}}|}{|Z_{\mathrm{v}}|}. \tag{2}$$

Here Z_{h} and Z_{v} is the radar reflectivity at horizontal and vertical polarization, respectively, and note that the unit for Z_{h} and Z_{v} is $\mathrm{mm^6 m^{-3}}$. In rain regions, Z_{DR} represents the oblateness of an average raindrop within a resolution volume of the radar. Large Z_{DR} values indicate the predominance of large raindrops in the resolution volume because air resistance causes a falling raindrop to become more ellipsoidal or oblate with increasing mass.

The correlation coefficient between the received signal intensities of the horizontally polarized wave and vertically polarized wave, ρ_{hv}, is expressed as,

$$\rho_{\mathrm{hv}} = \frac{|\langle n S_{\mathrm{hh}} S_{\mathrm{vv}}^* \rangle|}{\langle n |S_{\mathrm{hh}}|^2 \rangle^{\frac{1}{2}} \langle n |S_{\mathrm{vv}}|^2 \rangle^{\frac{1}{2}}} \tag{3}$$

where S_{hh} and S_{vv} are signal intensity of horizontally polarized wave and vertically polarized wave, respectively, and these in an angle bracket with n represent an expectation weighted by the number of particle. ρ_{hv} depends on the homogeneity of particles in the resolution volume and is sensitive to a melting layer. If the axis ratios of precipitation particles in the resolution volume are spatially and temporally similar, ρ_{hv} attains a large value close to 1.0.

If the raindrop shapes are not spatiotemporally uniform, or if a mixture of snowflakes, ice particles, and liquid particles exists such as in a melting layer, ρ_{hv} is less than 1.0 and perhaps below 0.95 in a melting layer (Illingworth and Caylor, 1991; Matrosov et al., 2007). Thus, ρ_{hv} is often treated as a parameter representing homogeneous precipitation particles within the resolution volume and is used to detect a melting layer. In rain regions, ρ_{hv} is generally greater than 0.97 (Doviak and Zrnić, 1993) and is reduced with increasing Z_{DR} (Bringi and Chandrasekar, 2001; Illingworth and Caylor, 1991). For the C band, Thurai et al. (2008) observed that reductions of ρ_{hv} in rain phases corresponded to the presence of large-diameter raindrops (shown as an increase in the mass-weighted mean diameter in their paper) and an increase in the width of the DSD. Thus, small ρ_{hv} values in rain phases represent the presence of large raindrops and a broad DSD ranging from small to large drops.

In this study, analyses of Z_{DR} and ρ_{hv} combining Z_{h} is useful to reveal the precipitation particle distribution in convective cells with low echo-top heights. The COBRA radar obtained these parameters during the observation.

1.3 DSD parameters

The polarimetric radar variables strongly relate to DSD, as expressed by above equations. Many researchers have studied DSD and DSD parameters, and then fit the DSD to a gamma model (Ulbrich, 1983):

$$N(D) = N_0 D^{\mu} exp(-\Lambda D), \tag{4}$$

where D is the drop diameter, N_0 is the intercept parameter, μ is the shape parameter, and Λ is the slope parameter. A method of the fitting to the gamma model by estimation of these parameters were described by Kozu and Nakamura (1991). Several previous reports have modeled the DSD as a normalized gamma form (e.g., Willis, 1984; Testud et al., 2000; Bringi et al., 2002; Gorgucci et al., 2002). The normalized gamma model can be expressed using D_0, N_w, and μ as follows:

$$N(D) = N_w f(\mu) \left(\frac{D}{D_0}\right)^{\mu} exp\left[-(3.67+\mu)\frac{D}{D_0}\right] \tag{5}$$

with

$$f(\mu) = \frac{6}{(3.67)^4}\frac{(3.67+\mu)^{\mu+4}}{\Gamma(\mu+4)}, \tag{6}$$

where N_w is the normalized intercept parameter of an equivalent DSD that has the same rain water content (W) and median volume diameter (D_0), and μ is the shape parameter in the gamma function. In the present study, like in many studies of DSD parameters (e.g., Bringi et al., 2003; Bringi et al., 2009), N_w and D_0 were estimated from polarimetric radar measurements to represent the DSD in convective cells. The D_0 indicates the representative size of raindrops in DSD, and the N_w indicates the representative number concentration of raindrops. D_0 is defined by

$$\frac{\pi\rho_w}{6}\int_0^{D_0} D^3 N(D) dD = \frac{W}{2}, \tag{7}$$

where ρ_w is the water density. The radar-estimated D_0 and N_w were obtained using the empirical relations of D_0 and $Z_{\rm DR}$ and the relationships among the radar reflectivity factor (Z), N_w, and D_0. These methods have been described in a number of past studies (e.g., Bringi et al., 2003; Thurai et al., 2008). The relationships are derived from ground-based measurements of DSDs. From the ground-based DSDs, D_0 is computed from μ and a slope parameter (Λ) in the gamma function:

$$D_0 = \frac{\mu + 3.67}{\Lambda}. \tag{8}$$

N_w in mm^{-1} m^{-3} is computed from D_0 in mm and W in g m^{-3} by

$$N_w = \frac{3.67^4}{\pi \rho_w} \left(\frac{10^3 W}{{D_0}^4} \right), \tag{9}$$

as given by Bringi and Chandrasekar (2001). Note that the unit for ρ_w is g cm^{-3}.

Comparing radar-measured polarimetric radar variables and ground-based DSD, qualitative precipitation particle information and quantitative size and number of raindrop are available. Using DSD parameters derived from ground-based DSD data, estimations of these DSD parameters based on polarimetric radar variables are available. Therefore, an observation that a polarimetric radar scans over a disdrometer is valid for comparing ground-based DSD measured by the disdrometer with polarimetric radar variables measured by the radar. We suggest that range height indicator (RHI), which has high resolution in height, directed to a disdrometer is very useful to analyze vertical structure of DSD in detail.

In this study, the purpose is clarification of spatial and size distribution pf precipitation particle and DSD parameters in convective cells with low echo-top height developing in a humid environment, with the goal of understanding microphysics and precipitation formation in the convective cells. For the purpose, we analyzed polarimetric radar vari-

ables and ground-based DSDs from our observation for convective cells developing in a humid environment, Okinawa Island during the Baiu period. On the basis of polarimetric radar variables, DSD parameters, D_0 and N_w, were estimated for the convective cells.

2 Observational data and method

2.1 Observation in the Baiu period of 2006

The COBRA radar (C band; 5.3 GHz) and ground-based instruments including disdrometers operated by NICT continuously performed observations at Okinawa Island during the Baiu period of 2006. From 4 to 11 June 2006, the intensive observation with sounding observations at Ogimi was conducted at Okinawa Island. Locations of instruments used for this study are shown in Fig. 2. The COBRA radar is located at Nago, Okinawa Island. Nakagawa et al. (2003) and Bringi et al. (2006) have described the radar in detail.

During the Baiu period of 2006, the COBRA radar performed plan position indicator (PPI) scanning of 14 elevations (0.5, 1.1, 1.8, 2.5, 3.3, 4.2, 5.3, 6.5, 8.1, 10.0, 12.3, 14.8, 17.4, and 20.5) every 6 min. In the intensive observation, the radar performed the PPI with the range height indicator (RHI) directed toward a disdrometer observation site (Ogimi: 41.2 degree azimuth angle) every 6 min to compare the radar-observed precipitation particle data with ground-based DSDs measured by the disdrometer. The RHI has a high resolution in vertical. Table 1 lists advanced settings of the radar observation. The radar had a 100-km radius of coverage for the PPI observations, as shown in Fig. 2. The range gate spacing of the PPI was approximately 300 m. The PPI rotation rate was 14.4 degrees per second (2.4 rpm). In the PPI scanning, the pulse width was 2.0 μs, the pulse repetition period was 1100 μs, and the number of integration pulses was 48. The RHI scanning was performed with range-gate spacing of 75 m and has higher resolution in range and vertical than PPI. In the RHI scanning, the pulse width was 0.5 μs, the pulse repetition period was 700 μs, and the number of integration pulses was 128. For

these observations, the transmitted polarization state was fixed at slant linear with tilt of 45 degrees. COBRA simultaneously transmitted and received horizontally and vertically polarized radar signals. There was good availability of Z_{h}, Z_{DR}, and ρ_{hv} for our analysis.

An impact-type disdrometer developed by Joss and Waldvogel (1967) (RD-69, Distromet) was used to measure DSD (number concentrations and diameters of raindrops) on the ground. The disdrometer is located at Ogimi, which is 14.8 km northeast of the COBRA radar along the 41.2 degree azimuth angle (Fig. 2). The impact-type disdrometer transforms the vertical momentum of an impacting drop into an electric pulse, the amplitude of which is a function of the drop diameter. Raindrops impacting the sensor surface with a sampling cross-sectional area of 50 cm^2 are sorted into 20 size classes ranging from 0.31 to 5.15 mm in equivalent diameter. From these observations, 1-minute DSD spectra were obtained from the number of counts in each of the 20 classes every 1 min. The RHI scanning was directed to the site of the disdrometer during the observation from 4 to 10 June. The radar-observed precipitation particle data and the ground-based DSD measured by the disdrometer were then compared.

2.2 Data processing

To correct the radar-observed Z_{h} and Z_{DR} ($Z_{\mathrm{h}}^{measured}$ and $Z_{\mathrm{DR}}^{measured}$) which might include attenuation, we considered specific attenuation at horizontal polarization (A_{h}) and specific differential attenuation between horizontal and vertical (A_{dp}) polarization. A_{h} and A_{dp} were obtained from Bringi et al's equations (Eqs. (4a) and (4b) in Bringi et

al., 2006) using specific differential phase ($K_{\rm DP}$):

$$A_{\rm h} = 0.0562 K_{\rm DP} \tag{10}$$

$$A_{\rm dp} = 0.0074 K_{\rm DP}^{1.13}. \tag{11}$$

The units for $A_{\rm h}$ and $A_{\rm dp}$ are dB km^{-1}. The relations of Bringi et al. (2006) was used for the attenuation procedure for COBRA and applicable for our cases. For the ith range gate, we obtain corrected $Z_{\rm h}$ and $Z_{\rm DR}$ ($Z_{\rm h}^{corrected}$ and $Z_{\rm DR}^{corrected}$):

$$Z_{\rm h}^{corrected}(i) = Z_{\rm h}^{measured}(i) + \Big(\sum_{j=0}^{j=i} 2A_{\rm h}(j)\delta r\Big) \tag{12}$$

$$Z_{\rm DR}^{corrected}(i) = Z_{\rm DR}^{measured}(i) + \Big(\sum_{j=0}^{j=i} 2A_{\rm dp}(j)\delta r\Big). \tag{13}$$

The $Z_{\rm h}$ and $Z_{\rm DR}$ used in this paper indicate the $Z_{\rm h}^{corrected}$ and $Z_{\rm DR}^{corrected}$, respectively. The corrected $Z_{\rm h}$ in PPI format was interpolated to a Cartesian grid with 1-km horizontal and 0.25-km vertical resolutions (constant altitude PPI: CAPPI), using weighted averaging (Cressman, 1959). The CAPPI was used for detection of convective cells.

For the $\rho_{\rm hv}$ in a simultaneous transmission, accuracies of ± 0.01 can be achieved when the number of integration pulses is greater than 25 (based on Fig. 5 of Liu et al., 1994). A large bias of $\rho_{\rm hv}$ is introduced by a low signal-to-noise ratio (SNR) less than 20 dB (Liu et al., 1994). Our observation included enough integration pulses (128 in RHI and 48 in PPI) to achieve accurate $\rho_{\rm hv}$. In addition, we focused on areas of large $Z_{\rm h}$ ($\geq$ 30 dBZ), which had large SNRs. Thus, the $\rho_{\rm hv}$ values in our study have sufficient accuracy to show features of the rain region.

For the impact-type disdrometer used in this study, a reduction in sensitivity for small drops occurs during and after large-drop impact (Sauvageot and Lacaux, 1995; Maki et al., 2001). During such "dead times," the number of smaller drops is underestimated.

Thus, we corrected the number of drops per class by equation (2) of Sheppard and Joe (1994):

$$C_j^* = C_j exp\Big\{\frac{0.035}{\Delta T}\sum_{D_k-0.085D_j}^{D_{20}} C_k \times ln[\frac{D_k}{0.85(D_j-0.25)}]\Big\}, \tag{14}$$

where C_j and C_j^* are the number of drops in channel j before and after correction, respectively. D_j is the mean diameter (mm) for the jth channel; and ΔT is the averaging periods (s).

For this study, a convective cell was extracted as a region of large radar reflectivity greater than 30 dBZ with a peak greater than 40 dBZ at 2 km above sea level (ASL) in CAPPIs; however, echoes in vertical cross sections that appeared to be trailing down from a melting layer were excluded because they could have been caused by melting ice particles rather than by convection. The threshold was established to be inclusive of mature convective cells but exclusive of stratiform rain areas. A convective cell with low echo-top height was defined as a convective cell for which an echo-top height of 30 dBZ was less than 6 km ASL in a CAPPI. Around Okinawa Island during Baiu periods, the environmental 0°C altitude is approximately 5 km ASL. The definition of the echo-top height is only 1 km higher than the environmental 0°C altitude. When the cores of convective cells accompanying the precipitation system passed over the disdrometer, we obtained RHI and ground-based DSD data for the cells. The RHI echo-top heights were estimated as the maximum altitude that 30-dBZ echoes were visible in convective cells in RHI scans.

For estimations of the 0°C altitude, we used sounding data obtained at Ogimi and Naha (Fig. 2). Sounding data at Ogimi were available from 4 to 10 June 2006. Data from soundings launched at Naha by the Japan Meteorological Agency were used after 10 June 2006.

In the observation period, a precipitation system consisting of a stratiform rain zone and a convective rain zone passed over Okinawa Island on 10 June 2006. Convective cells accompanied both the stratiform and convective rain zones. The precipitation system was associated with the Baiu front and was a typical Baiu frontal rainband. On 15 June 2006, isolated convective cells with low echo-top heights frequently occurred to the south of the Baiu front. First, we analysed precipitation particle distributions for convective cells in the convective rain zone of the rainband which were not been focused by previous studies and convective cells in the stratiform rain zone which have been recently proposed as typical convective cells around Okinawa Island during the Baiu period.

3 Convective cells accompanying a precipitation system

Characteristics of polarimetric radar variables and precipitation particle distribution in convective cells accompanying a Baiu frontal rainband have not been clarified in previous polarimetric radar analyses. A precipitation system associated the Baiu front passed over Okinawa Island on 10 June 2006 and was a typical Baiu frontal rainband around Okinawa Island. We investigated the characteristics of convective cells accompanying the precipitation system.

3.1 Precipitation system associated with the Baiu front

The Baiu front is recognized to the south of Okinawa Island on a surface weather chart at 0900 LST (LST = UTC + 9) on 10 June 2006 shown in Fig. 3. The Baiu front extends from east-northeast to west-southwest. Okinawa Island was in a very humid environment, which was shown in sounding data at Ogimi and Naha (Fig. 4). Relative humidity exceeded 70% below 5 km ASL. Especially, high humidity greater than 90% was found at lower altitude below 2 km ASL.

A precipitation system associated with the Baiu front is clearly shown in Fig. 5 which is the horizontal distributions of hourly rain intensities on 10 June 2006 around Okinawa Island, estimated by Japan Meteorological Agency (JMA) operational radar. The precipitation system, called a Baiu frontal rainband, extending from east-northeast to west-southwest to the north of the Baiu front over the East China Sea, moved northeastward and passed over Okinawa Island between 0600 and 1800 LST (Fig. 5). The

Baiu frontal rainband consisted of a convective rain zone along the southern edge of the rainband and a stratiform rain zone to the north of the convective rain zone. The convective rain zone containing meso-γ-scale convective cells appeared to be an intense rainfall region, approximately 80 km wide along the southern edge of the rainband (Fig. 5d). The stratiform rain zone was a broad, weak-rainfall region north of the convective rain zone. After the stratiform rain zone passed over Okinawa Island from 0600 to 1100 LST (Figs. 5a and 5b), the convective rain zone then passed over the island between 1200 and 1800 LST (Figs. 5c and 5d).

Environments surrounding the stratiform rain zone and the convective rain zone were observed by soundings. Figure 4a and 4b show vertical profiles of temperature, dew point temperature, relative humidity, wind speed and direction, potential temperature (θ), saturated equivalent potential temperature (θ_e^*), and equivalent potential temperature (θ_e) by a sounding at Ogimi at 0100 UTC June, 2006, when Ogimi was situated within the stratiform rain zone. Figure 4c and 4d show those by a sounding at Naha at 1200 UTC, when Naha was situated within the convective rain zone. In both environments of the stratiform and convective rain zones, high relative humidity larger than 70% was shown below 5 km ASL, especially, lower altitudes below 2 km ASL showed humid environments of 90% in relative humidity. The environment surrounding the stratiform rain zone showed that $d\theta_e^*/dz = 0$ approximately and θ_e was close to θ_e^*. The convective available potential energy (CAPE) of the environment for the stratiform rain zone (Fig. 4b) was very small. This profile represents a saturated neutral environment. For the convective rain zone, the CAPE was also small (less than 100 J kg^{-1}). This profile represents close to a saturated neutral environment (approximately $d\theta_e^*/dz = 0$). This environment that is saturated neutral is typical of the Baiu event within a precipitation

area.

Convective cells accompanying the rainband was also observed by the COBRA radar. Figure 6 shows typical examples of the stratiform and convective rain zones as horizontal distributions of $Z_{\rm h}$ at 2 km ASL in CAPPIs observed by COBRA. In the stratiform rain zone (Fig. 6a), convective cells, as shown by areas of dark shading ($\geq$ 40 dBZ), were embedded in large areas of stratiform rain. In the convective rain zone, other convective cells existed close to each other near the Baiu front (Fig. 6b). After convective cells in the stratiform rain zone passed over the disdrometer, convective cells in the convective rain zone passed over the disdrometer, and RHI data and ground-based DSD data were collected for the cores of several of these convective cells. We selected two of these cells that had similar features of large radar reflectivity and relatively low echo-top heights of 30 dBZ. These cells were scanned by RHI and passed over the disdrometer at their mature stages. One cell existed in the stratiform rain zone, and the other existed in the convective rain zone. Reflectivity of 30 dBZ indicates moderate rain intensity of approximately 3 mm h^{-1}.

3.2 Radar reflectivity of convective cells

Characteristics of radar reflectivity ($Z_{\rm h}$) of each of the selected convective cells is described in this section. Figure 7 illustrates the analyzed convective cells by CAPPI horizontal cross sections of $Z_{\rm h}$ at 2 km ASL and RHI vertical cross sections as each convective cell passed over the disdrometer. These convective cells developed at different times in the respective stratiform and convective rain zones. The cores of both convective cells passed over the disdrometer during their mature stages.

A convective cell, named CELL-A, in the stratiform rain zone passed over the dis-

drometer at approximately 0630 LST (Fig. 7a). The RHI showed that the convective cell had a 30-dBZ echo-top height of 5.6 km and a maximum $Z_{\rm h}$ of 50.6 dBZ at 3.2 km ASL at 0630 LST (Fig. 7b). The echo-top height was only 0.8 km above the environmental 0°C level (4.8 km ASL) observed by soundings at 1000 LST on the study day at Ogimi. CELL-A was embedded in a large area of stratiform rain that existed prior to the appearance of CELL-A. In this cell, convergences of Doppler velocity were recognized at lower altitude. This indicates a presence of updraft in the cell. Thus, this cell was a convection not a fallstreak echo. For over an hour, the 30-dBZ echo-top height of CELL-A in CAPPIs was almost always less than 6 km ASL, which was only approximately 1 km above the environmental 0°C level. The maximum radar reflectivity of CELL-A was 47.6 dBZ in a CAPPI at 0600 LST. Because large radar reflectivity greater than 45 dBZ in the cell continued for over 30 min (from 0542 to 0630 LST), the RHI scanning of CELL-A (0630 LST) occurred within the mature stage.

The other cell in the convective rain zone of the southern edge of the rainband was named CELL-B. This cell passed over the disdrometer at 1342 LST (Fig. 7c). The RHI showed a 30-dBZ echo-top height of 5.5 km and maximum $Z_{\rm h}$ of 56.1 dBZ at 1.2 km ASL at 1342 LST. Similar to CELL-A, the 30-dBZ echo-top height of CELL-B was also only 0.7 km above the environmental 0°C level. Around CELL-B, other convective cells developed and decayed in the convective rain zone. CELL-B developed with the low 30-dBZ (of CAPPIs) echo-top height less than 6 km ASL and was detected by radar for over an hour. The maximum reflectivity of CELL-B was 46.7 dBZ in a CAPPI at 1318 LST. Because large radar reflectivity greater than 45 dBZ continued for over 30 min (from 1312 to 1348 LST), the RHI scanning time was certainly within the mature stage of CELL-B. Both convective cells had similar characteristics of $Z_{\rm h}$: low 30-dBZ echo top

height of approximately 5.5 km ASL and large Z_{h}. These characteristics of Z_{h} are typical of convective cells developing around Okinawa Island during the Baiu periods.

4 Distribution of precipitation particles in convective cells

During the passage of convective cells over the disdrometer in their mature stages, the disdrometer measured DSD at Ogimi for each of the cells. The DSDs and rainfall intensity between 06 LST and 17 LST are shown in Fig. 8. The passages of CELL-A and CELL-B are indicated by two-headed arrows in this figure. The peaks of $N(D)$ and peaks of rainfall intensity corresponded approximately to the passages of convective cells. Each time of the passages of CELL-A and CELL-B over the disdrometer almost corresponded to the time of RHI scanning for each of the cell. Thus, it was available to compare the radar-measured precipitation particles data with the ground-based DSD measured by the disdrometer for each convective cell. Because the RHI had sufficient data for each convective cell, polarimetric radar variables were analyzed for three altitudes; higher (around 0°C level altitude), middle, and lower parts of convective cells. In this section, we clarify the precipitation particle distribution in CELL-A and CELL-B using the RHI and disdrometer data, and we also discuss the significance of the revealed distribution of precipitation particles in convective cells with relatively low echo-top heights in the Baiu periods.

4.1 Convective cell in the stratiform rain zone

To estimate spatial distribution of precipitation particle contributing to large Z_{h}, we analyzed polarimetric radar variables and Z_{h} using range bin data in an RHI of the COBRA observation. Figure 9 shows scatter diagrams of Z_{h} versus Z_{DR} and Z_{h} versus

$\rho_{\rm hv}$ for RHI range bin data of CELL-A within the rectangles (BOX-1, BOX-2, and BOX-3) given in Fig. 7b. Each box in Fig. 7b shows 2 km $\times$ 0.8 km (horizontal, vertical) areas in the RHI. At heights of 4.0−4.8 km (BOX-1), which almost correspond to the environmental 0°C altitude (4.8 km ASL) observed by a sounding at Ogimi at 0100 UTC on the study day, the maximum $Z_{\rm DR}$ exceeded 2.0 dB (Fig. 9a). In the same region, the minimum $\rho_{\rm hv}$ had a small value of 0.92 (Fig. 9d). The large $Z_{\rm DR}$ indicates that nonspherical particles predominated in the resolution volume of the radar. Around the 0°C level, $\rho_{\rm hv}$ values smaller than 0.95 indicate the presence of liquid and ice mixed-phase particles. These results suggest that wet snowflakes were present in CELL-A around heights of 4.0−4.8 km. In BOX-2 and BOX-3, $Z_{\rm DR}$ values were smaller than 1.5 dB with large $Z_{\rm h}$ ($\geq$ 35 dBZ) even close to 50 dBZ (Figs. 9b and 9c), and $\rho_{\rm hv}$ values were greater than 0.98 with the large $Z_{\rm h}$ (Figs. 9e and 9f). BOX-2 and BOX-3 show rain regions, as these areas were far below the 0°C level. The small $Z_{\rm DR}$ and large $\rho_{\rm hv}$ in the rain regions indicate that small raindrops predominated. That is, there was a high number concentration of small raindrops, which contributed to the large $Z_{\rm h}$.

To reveal the altitude variation of average vertical profiles, averaged $Z_{\rm DR}$ and $\rho_{\rm hv}$ for CELL-A are shown in Figs. 10a and 10b. These profiles were estimated from the $Z_{\rm DR}$ and $\rho_{\rm hv}$ averaged in the boxes shown in Fig. 10c using RHI data. To include the cell cores at every altitude, each box shows a RHI of 2 km $\times$ 0.4 km (horizontal, vertical), except for the lowest box which is 0.3 km in the vertical. The peak of averaged $Z_{\rm DR}$ was at approximately 4.2 km ASL and was close to the altitude of the minimum of averaged $\rho_{\rm hv}$ (4.6 km ASL) and the 0°C level. This result indicates the presence of melting precipitation particles. Below 3.5 km ASL, the averaged $Z_{\rm DR}$ had almost constant values between 1 and 1.5 dB, and $\rho_{\rm hv}$ was also constant at greater than 0.99. Below the environmental 0°C

level, a large number of small raindrops contributed to the large $Z_{\rm h}$ in CELL-A.

As CELL-A passed over Ogimi, the disdrometer measured intense rainfall for a short time as shown in Fig. 8. The rainfall intensity (R) derived from the temporally integrated DSD during the passage of CELL-A (for 10 minutes: 0627−0636 LST) was 19.4 mm h^{-1}, with a maximum of 44.6 mm h^{-1} in 1-minute integrated DSDs. Figure 11 shows the DSD during the passage of CELL-A. The DSD spectrum shown by the solid line, estimated from the 10-min integrated DSD for the passage of CELL-A, was fitted to a gamma function given by Eq. (4). For the fitting, using the equations for estimations of the DSD parameters reported by Kozu and Nakamura (1991), we calculated N_0, μ, and Λ from the temporally integrated DSD during the passage of the cell and then computed the gamma functions from these parameters. The radar reflectivity factor Z, calculated from the temporally integrated DSD during the passage of CELL-A, was 41.0 dBZ. The greatest number density was found for smaller raindrops with diameters of 1−2 mm; number densities of larger raindrops exceeding 3 mm in diameter were low. The ground-based DSD confirmed the predominance of a large number of small raindrops of 1−2 mm in diameter.

4.2 Convective cell in the convective rain zone

The scatter diagrams in Fig. 12 are similar to those in Fig. 9 except for CELL-B. At 4.0−4.8 km altitude (BOX-1), $Z_{\rm DR}$ was mostly smaller than 2.0 dB, with large $Z_{\rm h}$ greater than 40 dBZ (Fig. 12a). In the same box, $\rho_{\rm hv}$ showed small values with $Z_{\rm h}$ less than 45 dBZ. This indicates the presence of melting particles. With large $Z_{\rm h}$ greater than 45 dBZ, $\rho_{\rm hv}$ was greater than 0.97 and showed a feature of raindrops (Fig. 12d).

The $Z_{\rm DR}$ and $\rho_{\rm hv}$ values indicate that for CELL-B a large number of smaller raindrops contributed to the large $Z_{\rm h}$ in the core around the environmental 0°C level. At 2.5−3.3 km altitude (BOX-2), $Z_{\rm DR}$ values increased with increasing $Z_{\rm h}$; $Z_{\rm DR}$ greater than 1.5 dB predominated, with large $Z_{\rm h}$ greater than 43 dBZ (almost 40 dBZ) reaching a maximum of 2.6 dB (Fig. 12b). With the large $Z_{\rm h}$, $\rho_{\rm hv}$, which is generally reduced with increasing $Z_{\rm DR}$ (Illingworth and Caylor, 1991; Bringi and Chandrasekar, 2001), was smaller than 0.97 (Fig. 12e). At the lower altitudes of 1.0−1.8 km (BOX-3), $Z_{\rm DR}$ greater than 1.5 dB (with a maximum of 4 dB) predominated in areas of large $Z_{\rm h}$ greater than 40 dBZ (Fig. 12c). In those areas of large $Z_{\rm h}$, $\rho_{\rm hv}$ was small, with a minimum value of approximately 0.90 (Fig. 12f). Thurai et al. (2008) noted that reductions of $\rho_{\rm hv}$ in rain phases accompanied an increase in the width of the DSD range. For our case, the small $\rho_{\rm hv}$ far below the 0°C level represented the presence of large raindrops and a broad DSD ranging from small to large drops. At lower altitude, more larger raindrops were likely present and contributed to the large $Z_{\rm h}$ ($\geq$ 40 dBZ).

Variation of precipitation particle distribution with height was examined as the analysis of CELL-A. Figure 13 shows vertical profiles of $Z_{\rm DR}$, $\rho_{\rm hv}$, and $Z_{\rm h}$ for CELL-B (as in Fig. 10 for CELL-A). Below 4 km ASL, the averaged $Z_{\rm DR}$ was greater than 1 dB and increased with decreasing altitude (Fig. 13a). Particularly below 3 km ASL, $Z_{\rm DR}$ was greater than 1.5 dB. The averaged $\rho_{\rm hv}$, which decreased with increasing $Z_{\rm DR}$, was smaller than 0.98 (Fig. 13b). The peak of $Z_{\rm DR}$ value and the minimal $\rho_{\rm hv}$ value were shown below 2 km ASL (1.75 km). This result indicates that below the environmental 0°C level, larger raindrops were present at lower altitudes in CELL-B. The small $\rho_{\rm hv}$ implies a wide DSD, ranging from small raindrops with low fall velocities to large raindrops with greater fall velocities. Under this DSD, raindrops would grow in mass while falling

by collecting smaller raindrops. These profiles suggest that distinguishable coalescence processes of raindrops may exist in the lower altitudes.

While CELL-B passed over the disdrometer for 15 min (1331−1345 LST; Fig. 8) the disdrometer measured intense rainfall. The rainfall intensity (R) derived from the temporally integrated DSD during the passage (15 min) was 18.5 mm h^{-1}, with a maximum of 57.6 mm h^{-1} in 1-minute integrated DSDs. Figure 14 shows the DSD during the passage of CELL-B. The Z derived from the 15-min integrated DSD for the passage of CELL-B was 43.2 dBZ. The DSD extended to large-diameter drops of 4 mm with number density of 10^0 $mm^{-1}m^{-3}$. Compared to CELL-A, CELL-B had a lower number density of smaller raindrops (1−2 mm in diameter) but a larger number of raindrops exceeding 3 mm in diameter. The presence of large raindrops on the ground agrees with the results of polarimetric radar analyses below the environmental 0°C level in CELL-B. We confirmed the presence of large raindrops exceeding 3 mm in diameter on the ground during the passage of CELL-B.

4.3 Comparison of ground-based DSD between convective cell in the stratiform rain zone and convective cell in the convective rain zone

Comparing CELL-A in the stratiform rain zone with CELL-B in the convective rain zone, RHIs showed larger Z_{DR} and smaller ρ_{hv} for a given Z_h in CELL-B in areas of large Z_h greater than about 40 dBZ below the 0°C level. The differences in Z_{DR} and ρ_{hv} for a given Z_h imply differences in the DSD spectra. In CELL-A, smaller raindrops of high number concentrations contributed to the large Z_h; in CELL-B, larger raindrops

were present and contributed to the large $Z_{\rm h}$. The difference of DSDs shown in the polarimetric radar analysis was quantitatively compered using disdrometer data.

We confirmed the sizes of raindrops contributing to rainfalls using ground-based DSD data. The DSDs showed higher number densities of $1-2$ mm diameter raindrops for CELL-A and higher number densities of raindrops exceeding 3 mm in diameter for CELL-B, even though Z and R calculated from the temporally integrated DSD during the passage of each convective cell were almost the same; Z and R were 41.0 dBZ and 19.4 mm h^{-1} for CELL-A (Fig. 11) and 43.2 dBZ and 18.5 mm h^{-1} for CELL-B (Figure 14).

To verify the contributions of the DSDs to Z and R, we calculated the ratio of Z (RZ) and the ratio of R (RR) categorized by raindrop-diameter bins to Z and R, respectively. The ratios ($RZ(D_{a,b})$ and $RR(D_{a,b})$) were calculated by

$$RZ(D_{a,b}) = \left[\int_{D_a}^{D_b} D^6 N(D) dD / \int_{D_{min}}^{D_{max}} D^6 N(D) dD\right] \times 100, \tag{15}$$

and

$$RR(D_{a,b}) = \left[\frac{\pi}{6}\int_{D_a}^{D_b} D^3 N(D) V(D) dD / \frac{\pi}{6}\int_{D_{min}}^{D_{max}} D^3 N(D) V(D) dD\right] \times 100. \tag{16}$$

The values derived by (15) and (16) give the percentages of contributions by raindrops between D_a and D_b to Z and R, respectively. Here, $D_{\rm max}$ and $D_{\rm min}$ are the maximum and minimum diameters of observed raindrops during the passage of a cell, respectively; that is, the denominator of $RZ(D_{a,b})$ ($RR(D_{a,b})$) represents Z (R) estimated from the temporally integrated DSD during the passage. Furthermore, $V(D)$ is the fall velocity of a raindrop with diameter D, estimated using an empirical formula given by Atlas et al.

(1973). Tables 2 and 3 give the $RZ(D_{a,b})$ and $RR(D_{a,b})$ results, respectively. For CELL-B, larger raindrops exceeding 3 mm in diameter contributed a greater percentage (48%) to Z compared to their contribution percentage in CELL-A (8%). For CELL-A, smaller raindrops 1−2 mm in diameter made larger contributions (41%) than in CELL-B (16%), even though Z was almost the same in both convective cells. Similar contributions were found for R. For CELL-A, raindrops 1−2 mm in diameter made a large contribution to R (64%), whereas larger raindrops exceeding 3 mm in diameter contributed less (2%). In CELL-B, raindrops 1−2 mm in diameter made a smaller contribution to R, whereas those exceeding 3 mm in diameter (19%) made a larger contribution than in CELL-A.

Shusse et al. (2009) reported a study of polarimetric variables in convective cells developing with similar features of large reflectivity and low echo-top heights (of 30 dBZ) at approximately 5 km ASL in a humid environment. They analyzed $Z_{\rm DR}$ and $\rho_{\rm hv}$ and showed that, compared to an isolated convective cell, in a convective cell embedded in a stratiform precipitation area, smaller raindrops were predominant below 2 km ASL. The characteristics of polarimetric variables in the rain region of the embedded convective cell agree with those of CELL-A, in which large numbers of small raindrops of 1−2 mm in diameter predominated below the 0°C level. Meanwhile, the characteristics of polarimetric variables below 2 km ASL in the isolated convective cell were similar to those of CELL-B in the convective rain zone, which contained numerous large raindrops with diameters larger than 3 mm.

4.4 Verification of the polarimetric radar data

Comparing CELL-A in the stratiform rain zone with CELL-B in the convective rain zone with regard to parameters $Z_{\rm DR}$ and $\rho_{\rm hv}$, the parameters indicated that small raindrops made a large contribution to large $Z_{\rm h}$ in CELL-A, whereas larger raindrops contributed to large $Z_{\rm h}$ in CELL-B. The results correspond to the ground-based DSDs during the passages of each cell. For CELL-A, small raindrops $1-2$ mm in diameter made a large contribution to Z and R. For CELL-B, large raindrops exceeding 3 mm in diameter made a larger contribution to Z and R. We discuss the significance of the DSD features of CELL-A and CELL-B using polarimetric radar variables in PPIs in next section. To confirm the significance of the radar results, the accuracy of the radar data are checked in this section.

We compared the radar data from RHI observations with ground-based DSDs using $Z_{\rm h}$ (Z derived from DSD), $Z_{\rm DR}$, and D_0, to confirm that the radar results represented realistic DSDs. Table 4 lists the $Z_{\rm h}$ (Z), $Z_{\rm DR}$, and D_0 values of radar measurements and those of disdrometer measurements. The radar-measured $Z_{\rm h}$ and $Z_{\rm DR}$ and the calculated D_0 were averaged over the boxes at the lowest altitude shown in Figs. 10c and 13c using RHI data. The disdrometer-measured values given in Table 4 were maximum values derived from 1-minute integrated DSDs during the passages of each cell. The Z, $Z_{\rm DR}$, and D_0 derived from the 10-min integrated DSD for the passage of CELL-A and the 15-min integrated DSD for the passage of CELL-B are also listed within square brackets. The $Z_{\rm DR}$ value for the disdrometer was calculated using an expression given by Bringi and Chandrasekar (2001), for which we assumed the Rayleigh-Gans limit and axis ratios for the drops based on the model of Beard and Chuang (1987) for $D \geq 4$ mm and Pruppacher

and Beard (1970) for $D < 4$ mm.

The radar-measured $Z_{\rm h}$ of CELL-A and that of CELL-B were 44.8 dBZ and 48.5 dBZ, respectively. These values matched the maximum Z derived from the disdrometer DSD (45.5 dBZ and 49.6 dBZ, respectively). The radar-measured $Z_{\rm DR}$ at the lowest altitudes of CELL-A and CELL-B were 1.22 dB and 1.66 dB, respectively. These values were close to each maximum $Z_{\rm DR}$ calculated from the disdrometer DSD (1.25 dB and 1.66 dB, respectively). The measurement time of each maximum value of Z and $Z_{\rm DR}$ derived from the 1-minute integrated DSDs approximately corresponded to the time of RHI scans. The averaged D_0 value from radar measurements of CELL-A at the lowest altitudes was 1.84 mm, close to that derived from the 10-min integrated DSD for the passage of CELL-A (1.74 mm) rather than the maximum value of 1-minute integrated DSD. For CELL-B, the average D_0 calculated from radar data was 1.97 mm, which agreed with the D_0 derived from the disdrometer for the 15-min integrated DSD for the passage of CELL-B (1.98 mm). Thus, the radar variables reflected realistic DSDs in the convective cells; small raindrops with diameters of $1-2$ mm predominated in CELL-A, and a high number concentration of these small raindrops ($1-2$ mm in diameter) contributed to the large radar reflectivity ($\geq$ 40 dBZ), as shown by the ground-based DSD for CELL-A, in contrast, in CELL-B, large raindrops (over 3 mm in diameter) were present and contributed to the large radar reflectivity ($\geq$ 40 dBZ), as shown by the ground-based DSD for CELL-B.

The agreement between the radar-measured variables and those derived from the ground-based DSD might be explained as follows, considering the moist Baiu environment and the sounding observations. The soundings were launched at Ogimi at 0100 UTC when Ogimi was located in the stratiform rain zone (Fig. 4a), and at Naha at 1200 UTC

when Naha was located in the convective rain zone (Fig. 4c). These sounding observations showed high relative humidity exceeding 70% below 5 km ASL; particularly high humidity (above 90%) was found below 2 km ASL. Evaporation from raindrop surfaces was likely low during the fall of raindrops due to the highly humid environment. Therefore, the DSDs measured on the ground corresponded to the DSD within a convective cell over the ground-based measurement.

4.5 Statistical features of polarimetric radar variables in convective cells

To confirm the significance of the difference between raindrop distributions of the convective cells with low echo-top heights, namely numerous small raindrops in the convective cells in the stratiform rain zone and larger raindrops in the convective rain zone, we compared Z_{DR} versus Z_{h} and ρ_{hv} versus Z_{h} diagrams of convective cells in the stratiform rain zone with those of convective cells in the convective rain zone using PPI scanning data. Here we report analysis results for convective cells in the stratiform rain zone from volume scans at 0648 and 0706 LST, and in the convective rain zone from the volume scan at 1342 LST. Target convective cells had relatively low 30-dBZ echo-top heights less than 6.0 km ASL in CAPPIs. The radar range (r) for detecting convective cells was 10 km $\leq$ r $\leq$ 50 km, which was sufficient for collecting data between the low altitudes and echo-tops of convective cells. Figure 15 shows the frequency of 30-dBZ echo-top heights in CAPPIs for convective cells in the stratiform rain zone and in the convective rain zone. The CAPPIs for 0648 and 0706 LST showed 31 cells in the stratiform rain zone. Of the 31 total cells in the stratiform rain zone, 25 were convective cells with low

echo-top heights below 6.0 km. In the convective rain zone of the CAPPI for 1342 LST, 28 convective cells (from a total of 34) with low echo-top heights were found.

The DSD characteristics contributing large $Z_{\rm h}$ for a rain region were investigated by comparing $Z_{\rm DR}$ and $\rho_{\rm hv}$ values for a given $Z_{\rm h}$. Figure 16 shows the mean and frequency of $Z_{\rm DR}$ and $\rho_{\rm hv}$ versus $Z_{\rm h}$ every 5 dB for the rain region at lower altitude (below 3.0 km ASL) from range bin data of PPI scans obtained from convective cells with relatively low echo-top heights; specifically, the diagrams show the 25 cells in the stratiform rain zone (Figs. 16a, b) of Fig. 15a and the 28 cells in the convective rain zone (Figs. 16c, d) of Fig. 15b. The $Z_{\rm DR}$ and $\rho_{\rm hv}$ of range bin data of PPI scans were collected from 2-km horizontal columns centered around the cores of each of the convective cells between 0.7 km and 3.0 km ASL. The core was defined as the maximum reflectivity in CAPPIs at every 1-km altitude. Fig. 16 shows that for convective cells in the stratiform rain zone, more than 95% of $Z_{\rm DR}$ values were less than 1.5 dBZ with each $Z_{\rm h}$ bin less than 50 dBZ (Fig. 16a), and few $Z_{\rm DR}$ values were greater than 1.5 dB ($< 5\%$), even with larger $Z_{\rm h}$ close to 50 dBZ. Even with $Z_{\rm h}$ exceeding 50 dBZ, less than only 10% of $Z_{\rm DR}$ values were between 1.5 and 2.0 dB. For $\rho_{\rm hv}$, more than 95% of $\rho_{\rm hv}$ values for cells in the stratiform rain zone were greater than 0.98 with each $Z_{\rm h}$ bin (Fig. 16b). These distributions of $Z_{\rm DR}$ and $\rho_{\rm hv}$ in $Z_{\rm h}$ corresponded to those of CELL-A for the rain region. Therefore, the distribution characterized as a large number of small raindrops, like those found in CELL-A, was typical for cells with relatively low echo-top heights in the stratiform rain zone. For convective cells in the convective rain zone, in contrast to the cells in the stratiform rain zone, $Z_{\rm DR}$ values greater than 1.5 dB clearly occurred ($> 10\%$) in a region of $Z_{\rm h}$ greater than 40 dBZ (Fig. 16c). The $Z_{\rm DR}$ values greater than 2 dB were also clearly occurred in a region of $Z_{\rm DR}$ close to 50 dBZ. The $Z_{\rm DR}$ values for cells in the convective rain zone dramatically increased

with increasing $Z_{\rm h}$ and larger than those for cells in the stratiform zone for a given $Z_{\rm h}$. The mean $Z_{\rm DR}$ of convective cells in the convective rain zone showed large values for a given $Z_{\rm h}$ compared with convective cells in the stratiform rain zone. For the area of $Z_{\rm h}$ close to 40 dBZ, the mean $Z_{\rm DR}$ of cells in the convective zone was larger than that of cells in the stratiform zone. With the larger $Z_{\rm h}$ close to 50 dBZ, the mean $Z_{\rm DR}$ of cells in the convective zone was greater. The $Z_{\rm DR}$ distribution in $Z_{\rm h}$ and the trend of the mean $Z_{\rm DR}$ for cells in the convective rain zone represented characteristics of $Z_{\rm DR}$ distribution of CELL-B for the rain region. Figure 16d shows that cells with small $\rho_{\rm hv}$ values (< 0.98) were clearly found for the convective rain zone. The mean $\rho_{\rm hv}$ values of the convective rain zone were smaller than those of the stratiform rain zone for a given $Z_{\rm h}$. This $\rho_{\rm hv}$ distribution in $Z_{\rm h}$ of cells in the convective rain zone corresponded to that of CELL-B for the rain region. Therefore, convective cells with relatively low echo-top heights including larger raindrops, like CELL-B, generally occurred in the convective rain zone. These analyses confirm that the difference between the distribution of precipitation particle found in comparing CELL-A and CELL-B is a typical characteristic of precipitation particle distributions in convective cells with relatively low echo-top heights in stratiform and convective rain zones.

We have shown two types of precipitation particle distribution in convective cells: a large number of small raindrops for the stratiform rain zone and the presence of large raindrops in the convective rain zone. Shusse et al. (2009) also reported a difference in raindrop size in convective cells developing around Okinawa Island during a Baiu period. From their analyses of polarimetric variables, they showed the presence of smaller raindrops in a convective cell embedded in a stratiform rain region and the presence of larger raindrops in an isolated convective cell. The feature of predominant raindrops

in convective cells in the stratiform rain zone of our study (a large number of small raindrops) corresponds to that in the embedded convective cell described by Shusse et al. (2009). On the other hand, the feature of predominant raindrops in convective cells in the convective rain zone of our study is similar to that in the isolated convective cell described by Shusse et al. (2009) in that larger raindrops were predominant compared to the convective cells in the stratiform rain zone and the embedded convective cell. However, Z_{DR} values for the isolated convective cell described by Shusse et al. (2009) were slightly larger than the mean Z_{DR} for convective cells in the convective rain zone of our study, and larger raindrops than the average raindrop in the convective cells in the convective rain zone may have been present in the isolated convective cell. The variability of precipitation particle distribution in convective cells with low echo-top heights during Baiu periods is notable finding for an understanding on microphysics in convective cells developing in humid environments. To clarify the variation of the precipitation particle distribution among convective cells in the stratiform rain zone, convective cells in the convective rain zone, and isolated convective cells, quantitative estimation of the number and size of raindrops are required.

The convective cell embedded in the stratiform rain region shown by Shusse et al. (2009) is considered a convective cell in a stratiform rain zone from the point of view of radar reflectivity and polarimetric radar variables. On the basis of this consideration and reference of the previous studies, the representative convective cells with low echo-top heights around Okinawa Island in the Baiu are mentioned as "convective cells in the stratiform rain zone," "convective cells in the convective rain zone," and "isolated convective cells" from the perspective of precipitation particle distribution. There was a distinct difference in DSD characteristics among these types of convective cell. To exhibit

DSD characteristics in detail for these convective cells, clarification of DSD parameters indicating the number and size of raindrops, namely N_w and D_0 for the convective cells is important. In particular, it is important to confirm the temporal variations and spatial distributions of the DSD parameters (N_w and D_0) within the lifetime of convective cells to clarify the DSD characteristics and to understand the microphysics of convective cells developing during the Baiu.

5 Estimation of DSD parameters

In order to clarify the DSD characteristics and discuss conceivable microphysics of the convective cell with low echo-top heights, we estimated the D_0 and N_w from polarimetric radar measurement for the three types of convective cells as follows: "convective cells in the stratiform rain zone" of the Baiu frontal rainband of 10 June 2006, "convective cells in the convective rain zone" of the rainband, and "isolated convective cells" developing to the south of the Baiu front on 15 June 2006. For detailed analyses of time variation of DSD characteristics, we selected three convective cells developing over the sea and were observed by PPI volume scanning for their lifetimes. In this section, we demonstrate the estimated D_0 and N_w including the variations with time and height for each of the convective cells. For the estimation, we used empirical relations between polarimetric radar variables and DSD parameters obtained from disdrometer measurements.

5.1 Estimation of relations between DSD parameters and polarimetric radar variables

For estimations of D_0 from radar-measured $Z_{\rm DR}$, we used the following D_0-$Z_{\rm DR}$ relation given by Bringi et al. (2006):

$$\begin{aligned} D_0 &= 3.984\xi_{dr} - 3.2303; \qquad mm \\ &\text{for } \xi_{dr} \leq 1.3 \end{aligned} \tag{17}$$

$$\begin{aligned} &= 0.733\xi_{dr} + 0.9088; \qquad mm \\ &\text{for } \xi_{dr} > 1.3, \end{aligned} \tag{18}$$

where $Z_{\rm DR} = 10\log_{10}\xi_{dr}$. Bringi et al. (2006) estimated this D_0-$Z_{\rm DR}$ relation by a scattering calculation for a Baiu precipitation event using disdrometer data.

For estimations of N_w from radar variables, we used a relation among D_0, N_w and the radar reflectivity factor (Z) estimated from ground-based DSDs (1-min integration) measured by the disdrometer at Ogimi. Figure 17 shows disdrometer-measured D_0 versus Z/N_w along with the best fit curve:

$$\frac{Z}{N_w} = 0.0500{D_0}^{6.93}. \tag{19}$$

The ground-based DSD data used for estimating the above equation were acquired during precipitation with rainfall rate greater than 3 mm h^{-1} observed on 10 and 15 June 2006.

To check the accuracy of the estimated D_0 and N_w from polarimetric radar data, we compared the radar estimates and disdrometer-measurements of Z_h (Z), D_0, and N_w. Figure 18 shows time series of Z_h (Z), D_0, and N_w comparing radar estimates and disdrometer measurements during precipitation from 0630 LST to 1500 LST on 10 June 2006. The radar-measured Z_h and the radar-estimated D_0 and N_w were averaged using PPI data at an elevation angle of 1.1 degrees, extracted over the disdrometer site (a 1-km horizontal area) for Z_h greater than 20 dBZ. The disdrometer-measured values provided the 1-min integrated DSDs. The radar-measured Z_h and the radar-estimated D_0 were in good agreement with the disdrometer-measured Z and D_0, respectively. The radar-estimated N_w also showed agreement for Z_h greater than 30 dBZ, except for a few points, and for stratiform precipitation (from 0900 LST to 1230 LST). The good agreement in N_w is probably attributed to the Z-N_w-D_0 relation that was estimated for 3 mm h^{-1} (corresponding to approximately 30 dBZ) using 1-min integrated DSD data obtained from the disdrometer measurements.

5.2 DSD parameters estimated from polarimetric radar data

The estimation of DSD parameters from measured polarimetric radar variables was applied for representative convective cells in the humid environment: "convective cells in the stratiform rain zone" of the Baiu frontal rainband of 10 June 2006, "convective cells in the convective rain zone" of the rainband, and "isolated convective cells" developing to the south of the Baiu front on 15 June 2006. We investigated the estimated DSD parameters for cell lifetimes in detail for three typical convective cells selected from each of the three types.

5.2.1 Characteristics of DSD parameters for three types of convective cell

We analyzed one convective cell from each of three types of convective cells with low echo-top (30 dBZ) height less than 6 km ASL and intense reflectivity (>40 dBZ), using PPI volume scan data. The selected convective cells developed over the sea and were scanned in PPIs by the COBRA radar continuously for their lifetimes. Figure 19 shows the convective cells selected for the analyses; one was embedded in the stratiform rain zone of a Baiu frontal rainband of 10 June 2006 (Fig. 19a), another was located in the convective rain zone in the southern edge of the rainband (Fig. 19b), and the third was an isolated convective cell developing to the south of a Baiu front on 15 June 2006 (Fig. 19c). Each of the convective cells in Fig. 19 was in the mature stage when $Z_{\rm h}$ reached the maximum value in a CAPPI. These cells represented the convective cells embedded in the stratiform rain zone constituting the Baiu frontal rainband, the convective cells existing in the convective rain zone in the southern edge of the rainband, and the isolated convective cells, respectively, in $Z_{\rm DR}$ and $\rho_{\rm hv}$ features.

Vertical cross sections in the CAPPIs for the convective cells are also shown in Fig. 19. The cells had low echo-top heights. Echo top heights of 35 dBZ for these convective cells were about 4−5 km ASL, and echo-top heights of 30 dBZ were less than 6 km ASL. The 0°C altitude estimated from a sounding observation was 4.8 km ASL at 0100 UTC on 10 June 2006 at Ogimi, and that on 15 June 2006 at Naha was 4.9 km ASL at 1200 UTC. The altitude of 6 km ASL was only about 1 km above the 0°C altitude. The 30-dBZ echo-top height of each convective cell was less than 6 km ASL in the mature stage and continued at an altitude of less than 6 km ASL for the cell lifetime. Particularly, the 30-dBZ echo top height of the isolated convective cell was less than 5 km ASL for the lifetime.

The DSD parameters D_0 and N_w were estimated from polarimetric radar data in PPIs for three convective cells with low echo-top (of 30 dBZ) heights and intense reflectivity shown as Fig. 19. To examine DSD characteristics contributing to $Z_{\rm h}$, the estimated DSD parameters from range bin data of PPIs in a rain region (below 3.0 km ASL) were averaged every 5 dB in $Z_{\rm h}$. In the region below 3 km ASL, a clear difference in DSD characteristics was found between convective cells in the stratiform and convective rain zones. Figures 20a and 20b present the radar-estimated mean D_0 and mean $\log_{10}N_w$ versus $Z_{\rm h}$ every 5 dB, respectively, for the rain region for each of the convective cells. Data used in these figures were collected from PPI volume scans in the mature stage when the $Z_{\rm h}$ reached a maximum value for the lifetime in a CAPPI for each convective cell (at 0524 LST on 10 June for the convective cell in the stratiform rain zone, 1342 LST on 10 June for the convective cell in the convective rain zone, and 1854 LST on 15 June for the isolated convective cell). The volume scan time of PPI corresponded to the time of each CAPPI in Fig. 19. The D_0 values for the convective cell in the convective

rain zone and for the isolated convective cell were larger than those for the convective cell in the stratiform rain zone. The N_w values for the convective cell in the stratiform rain zone were higher than those for the other two cases. These D_0 and N_w for each of the convective cells were consistent with polarimetric radar variables reported in previous studies of convective cells with low echo-top heights in Baiu periods.

For the convective cell in the stratiform rain zone, the D_0 values did not reach 2 mm even when $Z_{\rm h}$ approached the large value of 50 dBZ, and D_0 was approximately 1.5 mm with $Z_{\rm h}$ of 45−50 dBZ (Fig. 20a). The D_0 values conformed to the features of polarimetric radar variables for convective cells in stratiform rain zones analyzed by the present study and Shusse et al. (2009). The N_w values for the convective cell were 32000−100000 mm^{-1} m^{-3} and were higher than those for the other two convective cells (Fig. 20b). These D_0 and N_w values indicate that a high number-concentration of small raindrops contributed to the large $Z_{\rm h}$ in the convective cell in the stratiform rain zone.

For the convective cell in the convective rain zone, the D_0 values dramatically increased with increasing $Z_{\rm h}$ (Fig. 20a). The D_0 values for a given $Z_{\rm h}$ were 0.5−0.7 mm larger than those for the convective cell in the stratiform rain zone. The D_0 was approximately 2 mm with $Z_{\rm h}$ of 40−45 dBZ and exceeded 2 mm with $Z_{\rm h}$ greater than 45 dBZ. The large D_0 was consistent with the features of polarimetric radar variables for convective cells in the convective rain zone presented by Section 4. On the other hand, N_w values for the convective cell in the convective rain zone were 1000−10000 mm^{-1} m^{-3}, and were less than those for the convective cell in the stratiform rain zone (Fig. 20b). The N_w values did not reach 10000 mm^{-1} m^{-3} even when $Z_{\rm h}$ was greater than 50 dBZ. This indicates that in the convective cell in the convective rain zone, large raindrops were predominant and contributed to the large $Z_{\rm h}$.

For the isolated convective cell, the maximum $Z_{\rm h}$ was smaller than that of the other cases, but the behaviors of D_0 and N_w with $Z_{\rm h}$ were similar to those for the convective cell in the southern edge; D_0 values were large (approximately 2 mm with $Z_{\rm h}$ 40−50 dBZ), and N_w values were low (1000−10000 mm^{-1} m^{-3}) compared with those of the convective cell in the stratiform rain zone. The $Z_{\rm h}$ for the isolated convective cell was small compared with the other cases; however, the D_0 was consistent with features of polarimetric radar variables for an isolated convective cell analyzed by Shusse et al. (2009). In the isolated convective cell, large raindrops were predominant and contributed to the large $Z_{\rm h}$ as well as the convective cell in the convective rain zone.

The characteristics of D_0 and N_w, estimated from the radar measurements, are represented in Fig. 20 for a mature stage in which $Z_{\rm h}$ reached its maximum value in each of the convective cells. To confirm that the difference in the radar-estimated D_0 and N_w among the convective cells was present throughout their lifetimes, time series of D_0 and N_w versus $Z_{\rm h}$ were investigated for each of the convective cells for a period of $Z_{\rm h}$ over 30 dBZ. Figures 21−23 show time series of the radar-estimated D_0 and $\log_{10} N_w$ averaged every 5 dBZ in $Z_{\rm h}$ versus $Z_{\rm h}$ for each of the convective cells with $Z_{\rm h}$ greater than or equal to 30 dBZ. The mean values for each PPI volume scan were calculated in the same way as for Fig. 20.

For the convective cell in the stratiform rain zone (Fig. 21), the D_0 values were smaller than 2 mm for most of the period, even when $Z_{\rm h}$ was over 40 dBZ. The N_w values were higher than 10000 mm^{-1} m^{-3}, and the maximum $Z_{\rm h}$ increased with increase in N_w, which reached 100000 mm^{-1} m^{-3}. Time series of the D_0 and $\log_{10} N_w$ versus $Z_{\rm h}$ for the convective cell in the convective rain zone are shown in Fig. 22. The D_0 values were over 1.5 mm throughout the period when $Z_{\rm h}$ was over 30 dBZ, and D_0 larger than

2 mm was found with $Z_{\rm h}$ exceeding 40 dBZ, especially in the first half of the period. The N_w values were less than 32000 mm^{-1} m^{-3} (about 4.5 on the logarithmic scale) in most of the period, even for $Z_{\rm h}$ over 50 dBZ. The time series of the D_0 and $\log_{10} N_w$ versus $Z_{\rm h}$ for the isolated convective cell are shown in Fig. 23. For the isolated convective cell, D_0 was larger than 1.5 mm throughout the period, and D_0 values were larger than 2.0 mm with $Z_{\rm h}$ greater than about 45 dBZ. Values of N_w were less than 10000 mm^{-1} m^{-3}. We confirmed that the D_0 values for the convective cell in the convective rain zone and for the isolated convective cell were larger than those for the convective cell in the stratiform rain zone at any given time; the N_w values for the convective cell in the stratiform rain zone were higher than those for the other two cases at any given time.

For the convective cell in the stratiform rain zone, a high number-concentration of small raindrops contributed to large $Z_{\rm h}$ throughout the cell lifetime. Thus, the DSD for the convective cell in the stratiform rain zone was characterized by a high number-concentration of small raindrops. In contrast, the DSDs for the convective rain zone in the convective rain zone and the isolated convective cell were characterized by large raindrops. Interestingly, these DSD characteristics for three convective cells suggest that for a given $Z_{\rm h}$, the convective cell in the stratiform rain zone contained larger rain water content compared with the other convective cells. Consideration of the different DSD characteristics is very important for a quantitative estimation of rain water content and rain intensity of the convective cells with low echo-top heights from radar data.

To confirm the spatial distributions of the DSD parameters, variations in $Z_{\rm h}$, D_0, and N_w with height were investigated. Figures 24−26 shows time series of vertical variations of the radar-measured $Z_{\rm h}$, radar-estimated D_0, and radar-estimated $\log_{10}N_w$ from PPI volume scan data throughout the lifetime of the convective cells (for a period of $Z_{\rm h}$ over

30 dBZ). These values of $Z_{\rm h}$, D_0, and N_w obtained from the PPIs were averaged every 0.5 km altitude. The PPI data were collected over 2-km horizontal columns centered around the core of a convective cell in CAPPIs at every altitude.

For the convective cell in the stratiform rain zone (Fig. 24), $Z_{\rm h}$ values greater than 46 dBZ were found at altitudes lower than 3 km ASL. The N_w values were higher than 32000 mm^{-1} m^{-3} at every altitude in the entire period and reached 100000 mm^{-1} m^{-3} at $Z_{\rm h}$ greater than 46 dBZ. In the large $Z_{\rm h}$ region, D_0 values were smaller than 2 mm. For the convective cell in the convective rain zone (Fig. 25), $Z_{\rm h}$ larger than 46 dBZ was found below 2 km ASL. In the large $Z_{\rm h}$ region, D_0 values were larger than 2 mm, and N_w values were less than 10000 mm^{-1} m^{-3}. Particularly below 2 km ASL, N_w was less and D_0 was large compared with respective values in the upper level of 2 km ASL. For the isolated convective cell (Fig. 26), D_0 larger than 2 mm were shown in altitudes below 3 km ASL, as well as the convective cell in the convective rain zone. In the larger D_0 region, N_w values were less than 10000 mm^{-1} m^{-3}. Although $Z_{\rm h}$ was not large compared with other two cases, D_0 values were larger than 2 mm in the area around the maximum $Z_{\rm h}$ (>42 dBZ), and D_0 larger than 1.5 mm continued through almost the entire period with $Z_{\rm h}$ over 30 dBZ. The core of large D_0 was located at altitudes below 2 km ASL for most of the lifetime. At the D_0 core, the N_w values had minima less than 1000 mm^{-1} m^{-3}. The isolated convective cell in this study was a shallow convection compared with the other two convective cells and the convective cells described by Shusse et al. (2009). However, the large D_0 values at altitudes below 2 km ASL in the isolated convective cell in this study are consistent with the polarimetric radar analyses for an isolated convective cell reported by Shusse et al. (2009). The DSD characterized by large D_0 is probably common in the isolated convective cells that develop around Okinawa Island during the

Baiu period.

5.2.2 Statistical features of estimated DSD parameters

To confirm the significance of the values of estimated D_0 and N_w for three convective cells, D_0 and N_w were estimated for 25 convective cells in the stratiform rain zone, for 28 convective cells in the convective rain zone, and for 14 isolated convective cells (Fig. 27). Samples for convective cells in the stratiform rain zone and those for convective cells in the convective rain zone is the same as Fig. 16. Isolated convective cells for the analysis were focused on convective cells, with 30-dBZ echo-top heights less than 6 km ASL, developing south to the Baiu front on 15 June 2006. The 14 isolated convective cells were collected from CAPPIs for 1554, 1624, 1654, 1848, and 1900 LST on 15 June. The radar range (r) for detecting the isolated convective cells was 10 km $\leq$ r $\leq$ 50 km, as well as the convective cells in the convective and stratiform rain zones shown in Fig. 15. The collected convective cells included cells in increasing-$Z_{\rm h}$ and decreasing-$Z_{\rm h}$ stages, not only those in the just mature stages. From the result of the analysis of estimated D_0 and N_w variation with cell lifetime (Figs. 21$-$23), a statistical analysis of D_0 and N_w with $Z_{\rm h}$ is available to combine PPI data of selected convective cells over 30 dBZ in $Z_{\rm h}$ for showing the differences among three types of convective cell in D_0 and N_w. The frequency every 5 dB in $Z_{\rm h}$ of D_0 and $\log_{10}N_w$ are shaded in Fig. 27. The D_0 and N_w were estimated from range bin data of PPI scans, which were collected from 2-km horizontal columns centered around the cores of each of the convective cells between 0.7 km and 3.0 km ASL. The core was defined as the maximum reflectivity in CAPPIs at every 1-km altitude. The method of the data sampling is the same as the analysis of Fig. 16. The estimated D_0 and $\log_{10}N_w$ from the PPI data were averaged every 5 dB in $Z_{\rm h}$ and shown

as solid line in Fig. 27.

The D_0 values for convective cells in the stratiform rain zone were smaller than those for the other two types for a given $Z_{\rm h}$. For the convective cells in the stratiform rain zone, more than 90% for D_0 values estimated from PPI data were smaller than 2 mm. The mean values every 5 dB were about 1.5 mm even $Z_{\rm h}$ reached 50 dBZ. For convective cells in the convective rain zone, mean D_0 values for a given $Z_{\rm h}$ were larger than those for the convective cells in the stratiform rain zone; the large frequency of D_0 were around 2 mm, and the mean D_0 values were approximately 2 mm around 50 dBZ in $Z_{\rm h}$. The frequency of D_0 larger than 2 mm increased to over 20% with $Z_{\rm h}$ greater than 45 dBZ (Fig. 27b). For isolated convective cells, the D_0 values for a given $Z_{\rm h}$ were larger than those for the convective cells in the stratiform rain zone; the values were approximately 2 mm around 50 dBZ in $Z_{\rm h}$. The values of N_w in Fig. 27 also agree with those for each of the three convective cells investigated in detail. The values of N_w for a given $Z_{\rm h}$ for the convective cells in the stratiform rain zone were smaller than those for the other two types with $Z_{\rm h}$ ranging from 30 dBZ to 55 dBZ. For the convective cells in the stratiform rain zone, large frequency of N_w ranged from 10000 to 320000 with $Z_{\rm h}$ larger than 45 dBZ. For the convective cells in the convective rain zone and for the isolated convective cells, large frequency of N_w ranged from 1000 to 32000 with $Z_{\rm h}$ around 45 dBZ. Therefore, the values of estimated D_0 and N_w for the three convective cells analyzed in detail had statistical significance for each type of convective cells.

6 Discussion

In the results of analyses of polarimetric radar variables and estimates of D_0 and N_w for three types of convective cells with low echo-top heights around Okinawa Island during the Baiu period, we suggest the variation of precipitation particle distribution in convective cells in the humid environment. On the basis of the estimated D_0 and N_w for three convective cells with low echo-top heights, we discuss conceivable microphysics for the convective cells. Additionally, we compare the values of the estimated D_0 and N_w with those shown in previous studies for different climate regimes.

6.1 Microphysics in convective cells

From analyses of time variation in D_0 and N_w for three representative convective cells, the DSD for each of the convective cells was characterized as follows. For the convective cell in the convective rain zone and for the isolated convective cell, D_0 showed large values and N_w showed low values compared with those for the convective cell in the stratiform rain zone at any given point in time. This result indicates that each of these three convective cells had different raindrop growth processes. From the variations in radar-estimated DSD parameters with the lifetimes of the three convective cells shown in Figs. 21−26, we discuss conceivable microphysics in each of those convective cells.

For large raindrops to exist in a convective cell, strong updraft might be required to sustain the large raindrops in the convective cell. We consider that one of the factor causing the different DSD is an intensity of updraft. An existence of updraft qualitatively identified by convergence from Doppler radar observations. The divergence of each of three convective cells was estimated using Doppler velocities at lower elevations. Here,

it is assumed that a convective cell has circular symmetry of velocity pattern. Using measured Doppler velocities at distance r_1 and r_2 from the radar in an azimuth angle (Vr_1 and Vr_2), we obtain

$$Div. = \left(\frac{Vr_2 - Vr_1}{r_2 - r_1}\right) \times 2, \tag{20}$$

where $r_2 > r_1$ is required. The divergence was estimated from the Doppler velocities measured at lower elevations (0.5−1.8 degrees) in PPIs passing through the area of each convective cell.

In the convective cell in the convective rain zone, large D_0 values (>2.0 mm) were located at altitudes below 3 km ASL during the early stage (Fig. 25). Below 2 km ASL in the convective cell, N_w values were smaller than those in the upper level. We focused on the early periods from 1336 LST to 1342 LST and from 1348 LST to 1354 LST, when $Z_{\rm h}$ increased with time below 2 km ASL. The D_0 values increased noticeably with increasing $Z_{\rm h}$. On the other hand, only small increases in N_w were estimated as $Z_{\rm h}$ increased. These variations indicate that raindrops collected smaller raindrops and grew larger. The small increases in N_w probably signify that water vapor was supplied at low altitudes by inflow, and cloud droplets then formed and grew into small raindrops. The characteristic of increasing D_0 with increased $Z_{\rm h}$ was clearly observed at altitudes below 2 km ASL in the convective cell during the early stages (1336−1342 LST and 1348−1354 LST). The process of raindrop size augmentation via the coalescence of raindrops over time was probably predominant at low altitudes during the early stage in the convective cell in the convective rain zone. For large raindrops to exist in a convective cell, strong updraft is required to sustain them. We considered an effect of updraft to forming large raindrops, on the basis of divergence estimated from Doppler velocity at lower altitudes. Figure 28 shows divergence estimated from Doppler velocity for the three convective cells.

For the convective cell in the convective rain zone, stronger convergence were estimated at the low altitudes (Fig. 28b), compared with that of the convective cell in the stratiform rain zone. The values of the convergence was about 20×10^{-3} s^{-1} at the altitudes below 1.0 km ASL. This suggests that stronger updraft seemed to present in the convective cells. We suggest that in the humid environment, raindrops formed at lower altitude below 0°C altitude by condensation; then the raindrops probably grew to a large size by coalescence of smaller raindrops, in the strong updraft at the lower altitude.

In general, a large raindrop (7−8 mm in diameter) breaks up in the air. Ulbrich and Atlas (2007) have reported that raindrop collision, coalescence, and breakup processes are predominant in a strong updraft, and generate the equilibrium DSDs. However, evidence of raindrop breakup, such as increased N_w and decreased D_0 with height, was not apparent in the D_0 and N_w distributions of the convective cell in the convective rain zone. Therefore, we believe that the raindrop breakup process was not predominant in the convective cell. Quantitative discussion of the breakup process and the relationships between raindrop size and the intensity and duration of updraft are topics for future research.

For the convective cell in the stratiform rain zone, below about 2 km ASL, as $Z_{\rm h}$ increased with time from 0500 LST to 0536 LST, N_w values increased significantly (Fig. 24). This indicates that a high number-concentration of small raindrops contributed preeminently to the increase in $Z_{\rm h}$ associated with the development of the convective cell. Also in this case, D_0 values were slightly larger and N_w values were slightly smaller than those at higher altitudes in the early stage (Fig. 24). This finding indicates that raindrop collision and coalescence processes occurred at the lowest altitudes in the convective cell. However, the evidence (increasing D_0 and decreasing N_w with height) was not

pronounced, as in the case of the convective cell in the convective rain zone. The estimated convergence for the convective cell in the stratiform rain zone was weaker than that for the convective cell in the convective rain zone (Fig. 28a). This indicates that the updraft in the convective cell in the stratiform rain zone seemed to be weaker. We suggest that in this convective cell in the stratiform rain zone, the increased number-concentration of raindrops over time may have occurred as follows. The cell probably developed in an area of preexisting cloud droplets in the weak stratiform rain zone. Coalescence of cloud droplets was effective for the growth of raindrops from numerous preexisting cloud droplets at altitudes below the 0°C level. The droplets probably increased in size and grew to raindrops. Fewer large raindrops formed in the convective cell in the stratiform rain zone, and the smaller raindrops fell through the weak updraft before they were able to grow larger.

For the convective cell in the convective rain zone and the convective cell in the stratiform rain zone, ice particles were probably present at upper altitudes above the 0°C altitude. However, we consider that the ice particles were minor and did not significantly affect the formation and growing processes of raindrops contributing large radar reflectivity below 0°C altitude in these convective cells, for the following reasons. The echo-top heights (30 dBZ) of the convective cells were less than 6 km ASL that only 1 km above the 0°C altitude. In addition, there was an evident convergence at lower altitude, meaning an existence of updraft, in the convective cells, and ice particles in the upper altitude could not fall down to lower altitude in the updraft.

For the isolated convective cell, the maximum D_0 corresponded to the minimum N_w below 2 km ASL (Fig. 26). As Z_{h} increased with time from 1848 LST to 1900 LST, D_0 increased and N_w decreased. In the isolated convective cell, DSDs characterized by large

raindrops contributed to the large Z_{h}, in contrast to the convective cell in the stratiform rain zone. For the isolated convective cell, which had large D_0 values as the convective cell in the convective rain zone, however, the estimated convergence was smaller (Fig. 28c). This indicates that strong updraft was not measure factor that large raindrops formed, at least for the isolated convective cell. We suggest a raindrop formation in the isolated convective cell as follows. Raindrops probably grew large via the coalescence of raindrops over time. The large raindrops were probably formed by collision and coalescence, and these processes were predominant at altitudes below 2 km ASL in the isolated convective cell.

Generally, the effect of raindrop evaporation in the sub-cloud layer is important for the consideration of raindrop size. We checked the environments where convective cells developed, using sounding data from Ogimi (0100 UTC on 10 June 2006; Fig. 4) and Naha (1200 UTC on 15 June 2006; not shown). These soundings indicated a humid environment with a relative humidity greater than 70% below 5 km ASL. In particular, below 2 km ASL, a very humid environment with a relative humidity above 85% was indicated. Therefore, the inflow of the convective cells was moist, and raindrop evaporation was probably low.

In this study, a formation and growing process of large raindrops in the convective cell in the convective rain zone was discussed from the analyses of the convergence which estimated from the Doppler velocity observed by single radar measurement. To quantitatively discuss the formation and growing process of raindrops and relations between raindrop size and intensity of updraft, quantitative estimation of updraft is necessary. A dual Doppler radar analysis is valid for the quantitative estimation of updraft and three dimensional structure of air flow. We suggest that an observation of dual polarimetric

Doppler radar is helpful for quantitative understanding of microphysics in convective cells. However, the result of the convergence analysis for the isolated convective cell showed that the strong updraft was not major factor which large raindrops formed in the convective cell. In order to understand microphysics in convective cells, we should consider other factor such as aerosol effects, the number of cloud nuclei, and mixing ratio of water vapour not only updraft. Considering these effects is helped by numerical simulations by a bin model, which predicts DSD in detail.

6.2 Comparison with other literature

In this study, we focused on DSD characteristics for individual convective cells in the environment of the Baiu period, and compared the DSD parameters for a given Z_{h}. This perspective differs from previous studies that classified DSD parameters between stratiform and convective rain types (e.g., , Tokay and Short, 1996; Bringi et al., 2009) and continental-like and maritime-like convective rain types (e.g., Bringi et al., 2003; Ulbrich and Atlas, 2007).

The quantitative estimation of D_0 and N_w for the three types of convective cells with low echo-top heights allows the estimated parameters to be compared to those of previous studies. As an example, we compare our results to those of previous studies showing that differences in D_0 and N_w for convective rain were related to whether the air mass environment was maritime or continental. The values of the DSD parameters for the convective cells in the stratiform rain zone (D_0 around 1.5 mm and N_w of $32000-100000$ mm^{-1} m^{-3}) were similar to those for Florida convective rain ("maritime-like") analyzed by Bringi et al. (2003) and relatively close to those for Brazil convective rain (Bringi

et al., 2003), whereas the D_0 and N_w values for the convective cells in the convective rain zone and for the isolated convective cells (D_0 around 2 mm and N_w of $1000-10000$ $\mathrm{mm^{-1}\ m^{-3}}$) were similar to those for Colorado convective rain ("continental-like"; Bringi et al., 2003) and tropical-continental storms (Ulbrich and Atlas, 2007). Nevertheless, comparison of the microphysics between our cases in the present study and convective rain in the above previous studies is difficult because the convective storms dealt with in these previous studies perhaps involved convective cells that developed to much higher altitudes and altitudes above 0°C.

We would like to suggest that the DSDs in the convective cells that develop around Okinawa Island during the Baiu period are characterized by each of the convective cell types observed in this study. To determine the causes contributing to the variability of the DSDs in individual cells, the importance of local updraft and the number of cloud condensation nuclei has been reported by many researchers (e.g., Atlas and Ulbrich, 2000; Knight et al., 2008). The effects of cloud condensation nuclei and the relationships between DSD and updraft intensity are subjects for future research.

7 Summary and conclusions

In order to clarify distributions of precipitation particles and DSD parameters in convective cells developing in a humid environment, we analyzed three types of convective cell with low echo-top heights around Okinawa Island during the Baiu period of 2006. We investigated radar-measured polarimetric radar variables and ground-based DSD measured by a disdrometer and estimated DSD parameters from the polarimetric radar variables using observational data from a C-band polarimetric radar and a disdrometer owned by the NICT.

For the analyses of polarimetric radar variables and ground-based DSD, we selected two convective cells associated with a Baiu frontal rainband, of 10 June 2006, which consisted of a convective rain zone along the Baiu front and a stratiform rain zone to the convective rain zone to the north of the convective rain zone. The selected two convective cells existing in each of the stratiform and convective rain zones were observed by RHIs when they passed over the disdrometer. Two types of precipitation particle distribution were revealed from the analyses of RHI scanning data and disdrometer-measured DSD. On the basis of results of the analyses, Fig. 29 illustrates the precipitation particle distributions of the two convective cells as characteristics raindrop distributions of convective cells accompanying the Baiu frontal rainband. Both convective cells had relatively low echo-top (30 dBZ) heights at approximately 5.5 km ASL with large radar reflectivity greater than 50 dBZ. The studied convective cell in the stratiform rain zone had an echo-top height of 5.6 km ASL, with a maximum Z_{h} of 51 dBZ. The studied cell in the convective rain zone had an echo-top height of 5.5 km ASL with a maximum Z_{h} of 56 dBZ. For the convective cell in the stratiform rain zone, analyses of polarimetric

radar variables showed that small raindrops predominated in the convective cell below the 0°C altitude; Z_{DR} was smaller than 1.5 dB, and ρ_{hv} was greater than 0.98, with large Z_{h} greater than 40 dBZ below 3.5 km ASL. The ground-based DSD showed high number densities of smaller raindrops (1−2 mm in diameter), with few raindrops exceeding 3 mm in diameter. Therefore, below the 0°C level, in the convective cell in the stratiform rain zone a large number of small raindrops 1−2 mm in diameter contributed to the large radar reflectivity. For the convective cell in the convective rain zone, analyses of polarimetric variables showed the presence of large raindrops below the 0°C level in the convective cell; Z_{DR} greater than 1.5 dB and ρ_{hv} smaller than 0.98 predominated, with large Z_{h} greater than 40 dBZ below 3 km ASL. The peak of Z_{DR} value and the minimal ρ_{hv} value were shown below 2 km ASL (1.75 km). The DSD from ground-based measurements showed large numbers of raindrops exceeding 3 mm in diameter. Therefore, below the 0°C level in the convective cell in the convective rain zone, large raindrops exceeding 3 mm in diameter were present and predominantly contributed to the large radar reflectivity. The significance of the two types of precipitation particle distribution were confirmed by the analysis of polarimetric radar variables in a rain region at lower altitude (below 3 km ASL) measured by PPIs for 25 cells in the stratiform rain zone and for 28 cells in the convective rain zone.

To investigated variations of DSD characteristics with time and height and to discuss the formation process of raindrops for three representative convective cells with low echo-top heights, D_0 and N_w were estimated for cell lifetime on the basis of polarimetric radar variables PPI volume scan data. The selected cells were three typical convective cells with low echo-top heights of 30 dBZ and less than 6 km ASL around Okinawa Island in the Baiu period: a convective cell in the stratiform rain zone of the Baiu frontal

rainband of 10 June 2006, a convective cell in the convective rain zone of the rainband, and an isolated convective cell developing to the south of the Baiu front on 15 June 2006. For detailed analyses of time variations, these selected convective cells developed over the sea and were observed by PPI volume scanning for their lifetimes. To examine DSD characteristics contributing $Z_{\rm h}$, the estimated DSD parameters from range bin data of PPIs in a rain region were averaged every 5 dB in $Z_{\rm h}$. The D_0 and N_w estimated from polarimetric radar measurements, involving the temporal and vertical variations of the DSD parameters within the lifetimes of the convective cells, demonstrated the DSD characteristics for each of the three convective cells. Figure 30 schematically shows each of the convective cells with the estimated D_0 and N_w in the mature stage and with DSD characteristics from the estimated D_0 and N_w. For the convective cell in the stratiform rain zone in the mature stage, the estimated D_0 was approximately 1.5 mm with $Z_{\rm h}$ of 45−50 dBZ and did not reach 2 mm even when $Z_{\rm h}$ approached a large value of 50 dBZ; the estimated N_w ranged from 32000 to 100000 mm^{-1} m^{-3}. This indicates that a high number-concentration of small raindrops contributed to large $Z_{\rm h}$ for the convective cell in the stratiform rain zone. For the convective cell in the convective rain zone in the mature stage, the estimated D_0 was approximately 2 mm with $Z_{\rm h}$ of 40−45 dBZ and exceeded 2 mm with $Z_{\rm h}$ greater than 45 dBZ; the estimated N_w were 1000−10000 mm^{-1} m^{-3}. This indicates that large raindrops contributed to large $Z_{\rm h}$ for the convective cell in the convective rain zone. For the isolated convective cell in the mature stage, D_0 was estimated to be approximately 2 mm with $Z_{\rm h}$ of 40−50 dBZ; the estimated N_w were also 1000−10000 mm^{-1} m^{-3}. This indicates that large raindrops contributed to large $Z_{\rm h}$ for the isolated convective cell. Analyses of these variations of estimated D_0 and N_w within the lifetimes of the convective cells indicate that the D_0 values for a given $Z_{\rm h}$ for the

convective cell in the convective rain zone and for the isolated convective cell were larger than those for the convective cell in the stratiform rain zone at any given time. The N_w values for the convective cell in the stratiform rain zone were larger than those for the other two cases at any given time.

From the variations of vertical structures of the radar-estimated D_0 and N_w with convective cell lifetime for the three convective cells, we suggested conceivable formation process of raindrops in each of the convective cells. For the convective cell in the stratiform rain zone, a high number-concentration of small raindrops contributed to increase of Z_{h}. This suggested that cloud droplets grew to small raindrops. For the convective cell in the convective rain zone and the isolated convective cell, larger D_0 and smaller N_w were shown below 2 km ASL in particular, and coalescence processes of raindrops were predominant at lower altitudes. We also suggested the relevance between raindrop size and intensity of updraft in the convective cells.

We also analyzed profiles of the radar-estimated D_0 and N_w for a given Z_{h} of 25 cells in the stratiform rain zone of the rainband, 28 cells in the convective rain zone of the rainband, and 14 isolated convective cells using PPI volume scan data. These analyses confirmed that characteristics of the estimated DSD parameters found in the each of the three convective cells generally occurred in each types of convective cells with relatively low echo-top heights in the Baiu period.

This study characterized precipitation particle distribution for three types of convective cells, with low echo-top heights, representing the humid environment as Okinawa Island during the Baiu period. In particular, the precipitation particle distributions for convective cells in the stratiform rain zone, which were obviously differ from convective cells in the convective rain zone and isolated convective cells, were newly characterized.

Additionally, we proposed the application for analyzing precipitation particle distribution and microphysics in convective cells using polarimetric radar and disdrometer. The precipitation particle distribution revealed from polarimetric radar measurements in this study provided valid directions for understanding microphysics and precipitation formation in convective cells developing in the humid environments.

Acknowledgement

I would like to express sincere acknowledgement to my supervisor, Prof. Hiroshi Uyeda, Hydrospheric Atmospheric Research Center (HyARC), Nagoya University for his passionate instruction and encouragement. I would like to thank Dr. Kazuhisa Tsuboki and Dr. Taro Shinoda, HyARC, Nagoya University, for their participation in fruitful discussions and their valuable suggestions, and members of Laboratory of Meteorology of HyARC for their assistance with the observations and data analyses. Thanks are extended to Prof. Kenji Nakamura, HyARC, Nagoya University, for his helpful suggestions and for giving me opportunity for participating the observations. I am grateful to Dr. Yukari Shusse, National Research Institute for Earth Science and Disaster Prevention, for her help in obtaining the data and providing fruitful advice on the polarimetric radar analyses. I am also grateful to Dr. David Allen Short, National Institute of Information and Communications Technology (NICT), for meaningful discussions. I am grateful to Prof. Dong-In Lee, Pkyong National University and Global Research Laboratory of Korea, for his encouragement regarding the observations and analyses. The instruments of the observation are owned by NICT. I acknowledge supports with NICT. Especially, scientists and engineers in the NICT supported the observations and our analyses. Sounding observations at Ogimi, Okinawa Island, were conducted in cooperation with the Lower Atmosphere and Precipitation Study (LAPS) project. This study was partly supported by the program "Formation of a virtual laboratory for diagnosing the earth's climate system" and a Grant-in-Aid for Scientific Research of the Japan Society for the Promotion of Science. Generic Mapping Tools software was used to draw the figures.

References

Akaeda, K., T. Yokoyama, M. I. A. Tabata and H. Sakakibara, 1991: Evolution of the kinematic structure within a meso-β-scale convective system in the growing and mature stages. *Mon. Wea. Rev.*, **119**, 2664–2676.

Atlas, D., R. C. Srivastava and R. S. Sekhon, 1973: Doppler radar characteristics of precipitation at vertical incidence. *Rev. Geophys.*, **11**, 1–35.

Atlas, D. and C. W. Ulbrich, 2000: An observationally based conceptual model of warm oceanic convective rain in the tropics. *J. Appl. Meteorol.*, **39**, 2165–2181.

Atlas, D. and C. Ulbrich, 2006: Drop size spectra and integral remote sensing parameters in the transition from convective to stratiform rain. *Geophys. Res. Letts.*, **33**, L16803.

Atlas, D. and C. R. Williams, 2003: The anatomy of a continental tropical convective storm. *J. Atmos. Sci.*, **60**, 3–15.

Beard, K. V. and C. Chuang, 1987: A new model for the equilibrium shape of raindrops. *J. Atmos. Sci.*, **44**, 1509–1524.

Bringi, V. N., D. A. Burrows and S. M. Menon, 1991: Multiparameter radar and aircraft study of raindrop spectral evolution in warm-based clouds. *J. Appl. Meteorol.*, **30**, 853–880.

Bringi, V. N. and V. Chandrasekar, 2001: Polarimetric Doppler weather radar: Principles and applications. *Cambridge University Press*, 636pp.

Bringi, V. N., G. J. Huang, V. Chandrasekar and E. Gorgucci, 2002: A methodology for estimating the parameters of a gamma raindrop size distribution model from polarimet-

ric radar data: Application to a squall-line event from the TRMM/Brazil campaign. *J. Atmos. Oceanic Technol.*, **19**, 633–655.

Bringi, V. N., V. Chandrasekar, J. Hubbert, E. Gorgucci, W. L. Randeu and M. Schoenhuber, 2003: Raindrop size distribution in different climatic regimes from disdrometer and dual-polarized radar analysis. *J. Atmos. Sci.*, **60**, 354–365.

Bringi, V. N., M. Thurai, K. Nakagawa, G. J. Huang, T. Kobayashi, A. Adachi, H. Hanado and S. Sekizawa, 2006: Rainfall estimation from C-band polarimetric radar in Okinawa, Japan: Comparisons with 2D-video disdrometer and 400 MHz wind profiler. *J. Meteor. Soc. Japan*, **84**, 705–724.

Bringi, V. N., C. R. Williams, M. Thurai and P. T. May, 2009: Using dual-polarized radar and dual-frequency profiler for DSD characterization: A case study from Darwin, Australia. *J. Atmos. Oceanic Technol.*, **26**, 2107–2122.

Cressman, G. P., 1959: An operational objective analysis system. *Mon. Wea. Rev.*, **87**, 367–374.

Doviak, R. J. and D. S. Zrnić, 1993: Doppler radar and weather observations, 2nd edition. *Academic Press, San Diego, CA*, 562.

Gorgucci, E., V. Chandrasekar, V. N. Bringi and G. Scarchilli, 2002: Estimation of raindrop size distribution parameters from polarimetric radar measurement. *J. Atmos. Sci.*, **59**, 2372–2384.

Hashimoto, A. and T. Harimaya, 2005: Characteristics of raindrop size distribution dependent on the life stage of a convective precipitation cloud in the Baiu season. *J. Meteor. Soc. Japan*, **83**, 641–649.

Illingworth, A. J. and I. J. Caylor, 1991: Co-polar correlation measurements of precipitation. *Proceeding 25th Conf. on Radar Meteorol.*, 650–653, Paris, France, Amer. Meteor. Soc.

Joss, J. and A. Waldvogel, 1967: Ein spectrograph für niedersclagstropfen mit automatischer auswertung. *Pure Appl. Geophys*, **68**, 240–246.

Kato, T., S. Hayashi and M. Yoshizaki, 2007: Statistical study on cloud top heights of cumulonimbi thermodynamically estimated from objective analysis data during the Baiu season. *J. Meteor. Soc. Japan*, **85**, 529–557.

Knight, C. A., L. J. Miller and R. A. Rilling, 2008: Aspects of precipitation development in trade wind cumulus revealed by differential reflectivity at S band. *J. Atmos. Sci.*, **65**, 2563–2580.

Kozu, T., K. K. Reddy, S. Mori, M.Thurai, J. T. Ong, D. N. Rao and T. Shimomai, 2006: Seasonal and diurnal variations of raindrop size distribution in Asian monsoon region. *J. Meteor. Soc. Japan*, **84A**, 195–209.

Kozu, T. and K. Nakamura, 1991: Rainfall parameter estimation from dual-radar measurements combining reflectivity profile and path-integrated attenuation. *J. Atmos. Oceanic Technol.*, **8**, 259–270.

Liu, L., V. N. Bringi and V. Chandrasekar, 1994: Analysis of the copolar correlation coefficient between horizontal and vertical polarizations. *J. Atmos. Oceanic Technol.*, **11**, 950–962.

Maki, M., T. D. Keenan, Y. Sasaki and K. Nakamura, 2001: Characteristics of the rain-

drop size distribution in tropical continental squall lines observed in Darwin, Australia. *J. Appl. Meteorol.*, **40**, 1393–1412.

Matrosov, S. Y., K. A. Clark and D. E. Kingsmill, 2007: A polarimetric radar approach to identify rain, melting-layer, and snow regions for applying corrections to vertical profiles of reflectivity. *J. Appl. Meteor. Climatol.*, **46**, 154–166.

Nakagawa, K., H. Hanado, S. Satoh, N. Takahashi, T. Iguchi and K. Fukutani, 2003: Development of a new C-band bistatic polarimetric radar and observation of typhoon events. *Proc. 31st Conf. on Radar Meteor.*, Vol. 2, 863–866, Seattle, Amer. Meteor. Soc.

Ninomiya, K., T. Akiyama and M. Ikeda, 1988: Evolution and fine structure of a long-lived meso-α-scale convective system in Baiu frontal zone. Part I: Evolution and meso-β-scale characteristics. *J. Meteor. Soc. Japan*, **66**, 331–350.

Ninomiya, K. and T. Akiyama, 1992: Multi-scale features of Baiu, the summer monsoon over Japan and the East Asia. *J. Meteor. Soc. Japan*, **70**, 467–495.

Pruppacher, H. R. and K. V. Beard, 1970: A wind tunnel investigation of the internal circulation and shape of water drops falling at terminal velocity in air. *Quart. J. Roy. Metor. Soc.*, **96**, 247–256.

Sauvageot, H. and J. P. Lacaux, 1995: The shape of averaged drop size distributions. *J. Atmos. Sci.*, **52**, 1070–1083.

Sheppard, B. E. and P. I. Joe, 1994: Comparison of raindrop size distribution measurements by Joss-Waldvogel disdrometer, a PMS 2DG spectrometer, and POSS Doppler radar. *J. Atmos. Oceanic Technol.*, **11**, 874–887.

Shinoda, T., R. Maki, S. Shimizu, K. Tsuboki and H. Uyeda, 2007: Statistical features of precipitation cells observed in East Asia during the Meiyu/Baiu period. Preprints, *Conf. on Mesoscale Meteorology and Typhoon in East Asia (ICMCS-VI)*, 199–203.

Shusse, Y., K. Nakagawa, N. Takahashi, S. Satoh and T. Iguchi, 2009: Characteristics of polarimetric radar variables in three types of rainfalls in a Baiu front event over the East China Sea. *J. Meteor. Soc. Japan*, **87**, 865–875.

Testud, J., E. L. Bouar, E. Obligis and M. Ali-Mehenni, 2000: The rain profiling algorithm applied to polarimetric weather radar. *J. Atmos. Oceanic Technol.*, **17**, 332–356.

Thurai, M., D. Hudak and V. N. Bringi, 2008: On the possible use of copoler correlation coefficient for improving the drop size distribution estimations at C band . *J. Atmos. Oceanic Technol.*, **25**, 1873–1880.

Tokay, A. and D. A. Short, 1996: Evidence from tropical raindrop spectra of the origin of rain from stratiform versus convective clouds. *J. Appl. Meteorol.*, **35**, 355–371.

Ulbrich, C. W., 1983: Natural variations in the analytical form of the raindrop size distribution. *J. Appl. Meteorol.*, **22**, 1764–1775.

Ulbrich, C. W. and D. Atlas, 2007: Microphysics of raindrop size spectra: Tropical continental and maritime storms. *J. Appl. Meteor. Climatol.*, **46**, 1777–1791.

Wang, J. J. and L. D. Carey, 2005: The development and structure of an oceanic squall-line system during the South China Sea Monsoon Experiment. *Mon. Wea. Rev.*, **133**, 1544–1561.

Willis, P. T., 1984: Functional fits to some observed drop size distributions and parameterization of rain. *J. Atmos. Sci.*, **41**, 1648–1661.

Yuter, S. E. and R. A. Houze Jr., 1995: Three dimensional kinematic and microphysical evolution of Florida cumulonimbus. Part II: Frequency distributions of vertical velocity, reflectivity, and differential reflectivity. *Mon. Wea. Rev.*, **123**, 1941–1963.

Zhang, C. Z., H. Uyeda, H. Yamada, B. Geng and Y. Ni, 2006: Characteristics of mesoscale convective systems over East part of continental China during the Meiyu from 2001 to 2003. *J. Meteor. Soc. Japan*, **84**, 763–782.

Tables and Figures

Table. 1. Plan position indicator (PPI) and range height indicator (RHI) settings of the COBRA radar observation.

	Plan position indicator (PPI)	Range height indicator (RHI)
Number of elevations	14 [0.5, 1.1, 1.8, 2.5, 3.3,	
[Elevation angles]	4.2, 5.3, 6.5, 8.1, 10.0,	
	12.3, 14.8, 17.4, and 20.5 (degrees)]	
Direction in azimuth angle		41.2 degree
Radar coverage in radius	100 km	35 km
		(from 0 to 55 degrees in elevation)
Rotation rate	2.4 rpm (14.4° sec^{-1})	
Range gate spacing	300 m	75 m
Beam spacing	1 degree	0.4 degree
Pulse width	2.0 μs	0.5 μs
Pulse repetition period	1100 μs	700 μs
Number of integration pulses	48	128
Nyquist velocity	12.8 m s^{-1}	21 m s^{-1}

Table. 2. Ratios of the radar reflectivity factor (RZ) categorized by raindrop diameter bins to the radar reflectivity factor. Raindrop diameters (D) are categorized as $D < 1$ mm, 1 mm $\leq D < 2$ mm, 2 mm $\leq D < 3$ mm, 3 mm $\leq D < 4$ mm, and 4 mm $\leq D$.

	RZ [%]	
DIAMETER(D) [mm]	CELL-A	CELL-B
$0 < D < 1$	0.3	0.2
$1 \leq D < 2$	40.7	16.0
$2 \leq D < 3$	51.3	35.4
$3 \leq D < 4$	7.7	42.9
$4 \leq D$	0.0	5.5

Table. 3. As in Table 2, but for rainfall intensity (RR).

DIAMETER(D) [mm]	RR [%] CELL-A	CELL-B
$0 < D < 1$	2.3	2.4
$1 \leq D < 2$	63.9	44.0
$2 \leq D < 3$	31.5	34.7
$3 \leq D < 4$	2.3	17.8
$4 \leq D$	0.0	1.1

Table. 4. Comparisons of radar data with disdrometer data for $Z_{\rm h}$ (Z derived from disdrometer data), $Z_{\rm DR}$, and D_0 of CELL-A and CELL-B. The radar-measured values were areally averaged over a box of 2 km $\times$ 0.3 km (horizontal, vertical) at the lowest altitudes of each of Figures 10c and 13c using RHI data. The disdrometer-measured values show the maximum derived from 1-minute integrated DSDs during the passages of each cell. The parenthetical values for radar data show the standard deviation. For the disdrometer data, values calculated from the 10-min integrated DSD for the passage of CELL-A and 15-min integrated DSD for the passage of CELL-B are also shown in square brackets.

PARAMETER	CELL-A		CELL-B	
	RADAR	DISDROMETER	RADAR	DISDROMETER
$Z_{\rm h}$ (Z) [dBZ]	44.8(2.29)	45.5 [41.0]	48.5(3.02)	49.6 [43.2]
$Z_{\rm DR}$ [dB]	1.22(0.31)	1.25 [0.95]	1.66(0.48)	1.66 [1.37]
D_0 [mm]	1.84(0.19)	2.37 [1.74]	1.97(0.22)	2.63 [1.98]

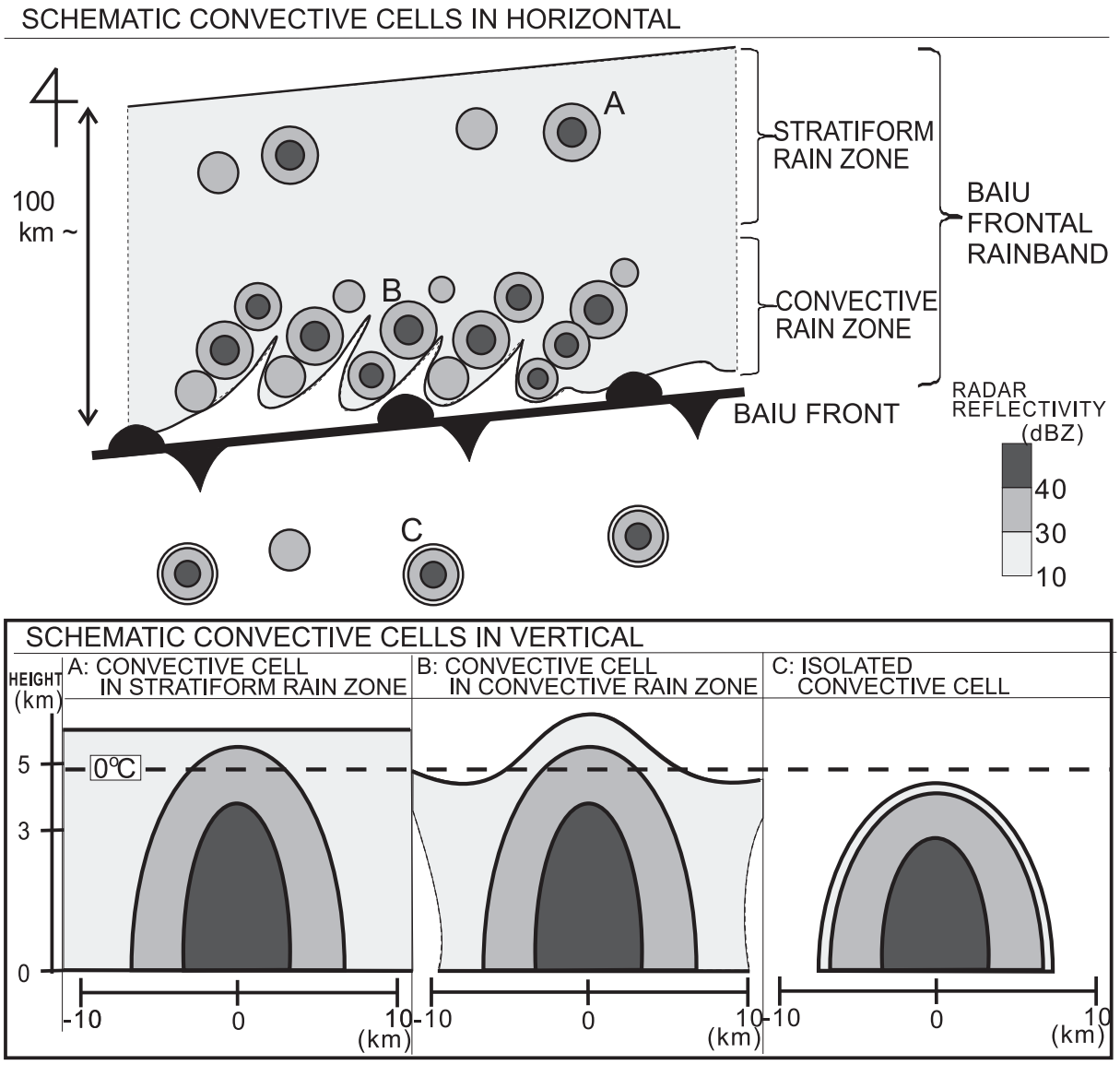

Fig. 1. Schematic convective cells representing convective cells with low echo-top heights in the Baiu around Okinawa Island. (top) Horizontal distribution with the radar reflectivity of each of the convective cells to the Baiu front. (bottom) Vertical cross section in radar reflectivity of each of the convective cells: (left) convective cell in stratiform rain zone, (middle) convective cell in convective rain zone, and (right) isolated convective cell. Shading represents the radar reflectivity. Convective cells are indicated by areas over 30 dBZ. Large reflectivity (greater than 40 dBZ) areas within convective cells are shaded in black. Dashed line represents the 0°C altitude.

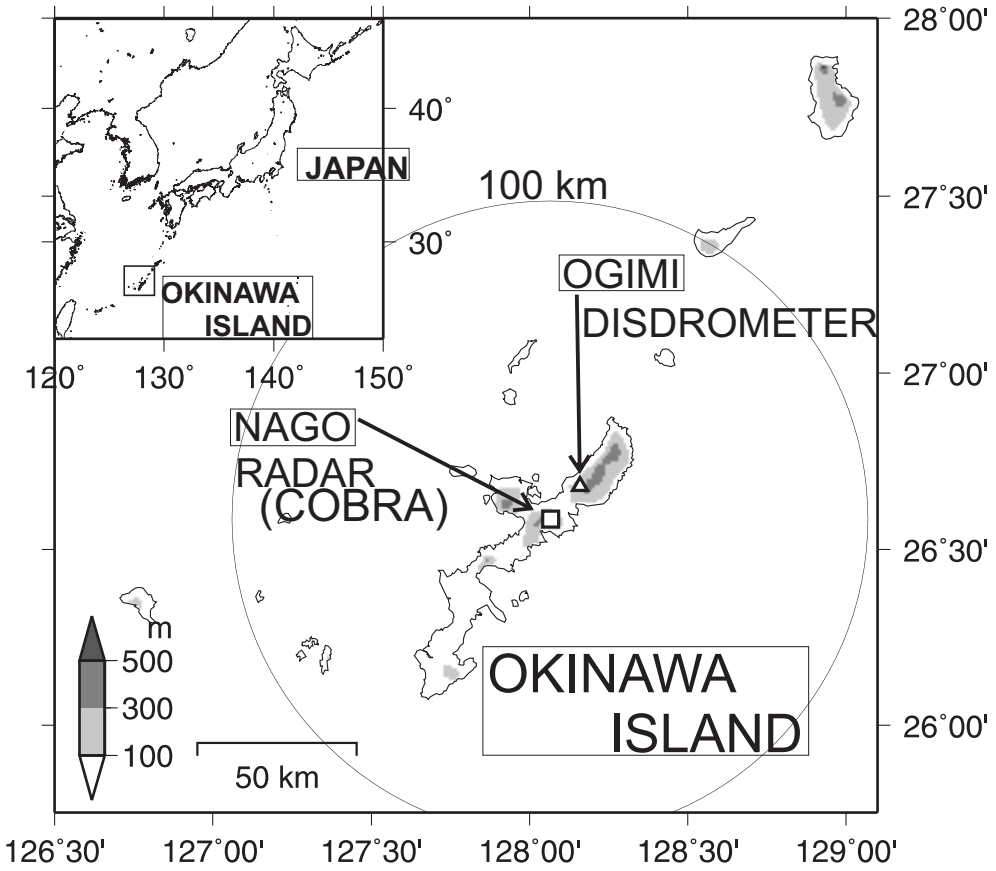

Fig. 2. Location of Okinawa Island and the instrument sites. An open square and an open triangle denote the radar and disdrometer locations, respectively. The large circle presents the 100-km radar observation range. Shading represents the terrain.

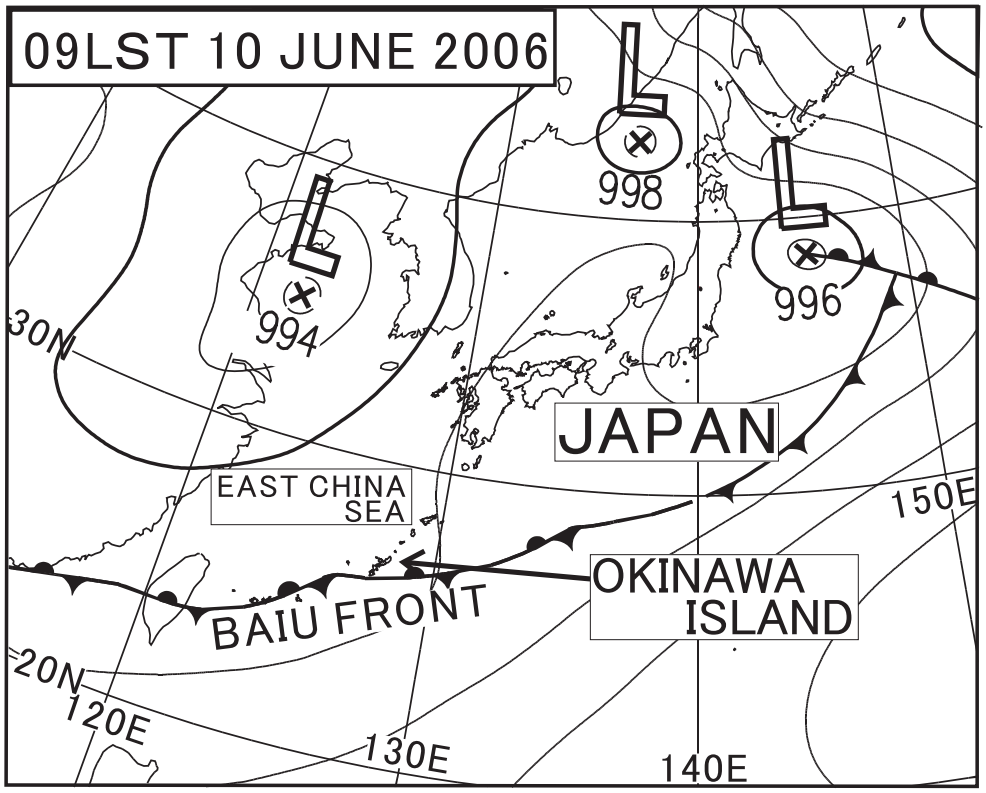

Fig. 3. Surface weather chart around Japan at 0900 LST 10 June 2006.

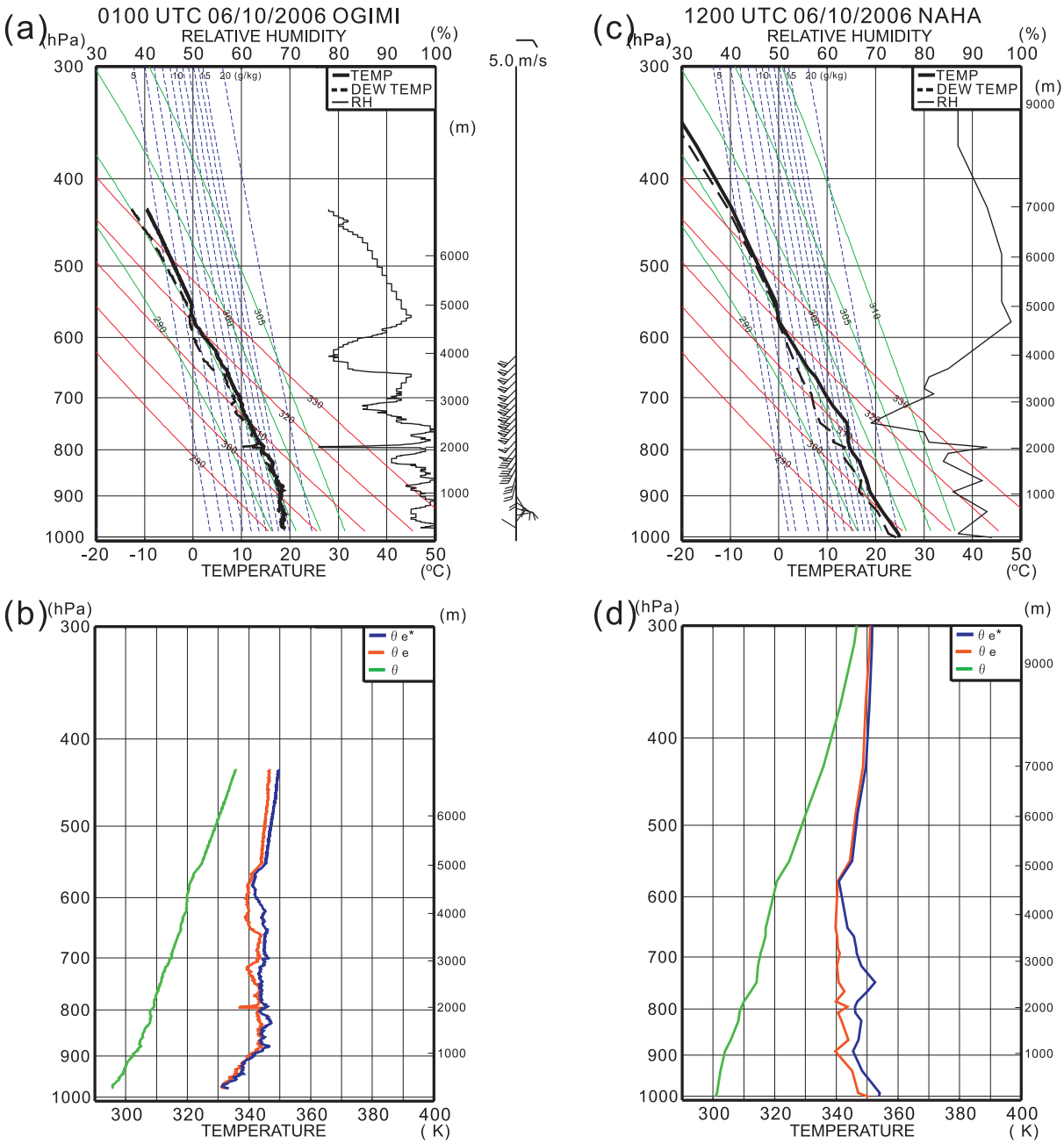

Fig. 4. Vertical profiles of (a) temperature (thick lines), dew point temperature (dashed lines), relative humidity (thin lines), wind speed and direction (on the right), (b) potential temperature (green lines), equivalent potential temperature (red lines), and saturated equivalent potential temperature (blue lines) observed by a sounding at Ogimi at 0100 UTC. (c) and (d) are the same as (a) and (b), respectively, but for observation at Naha at 1200 UTC without wind data.

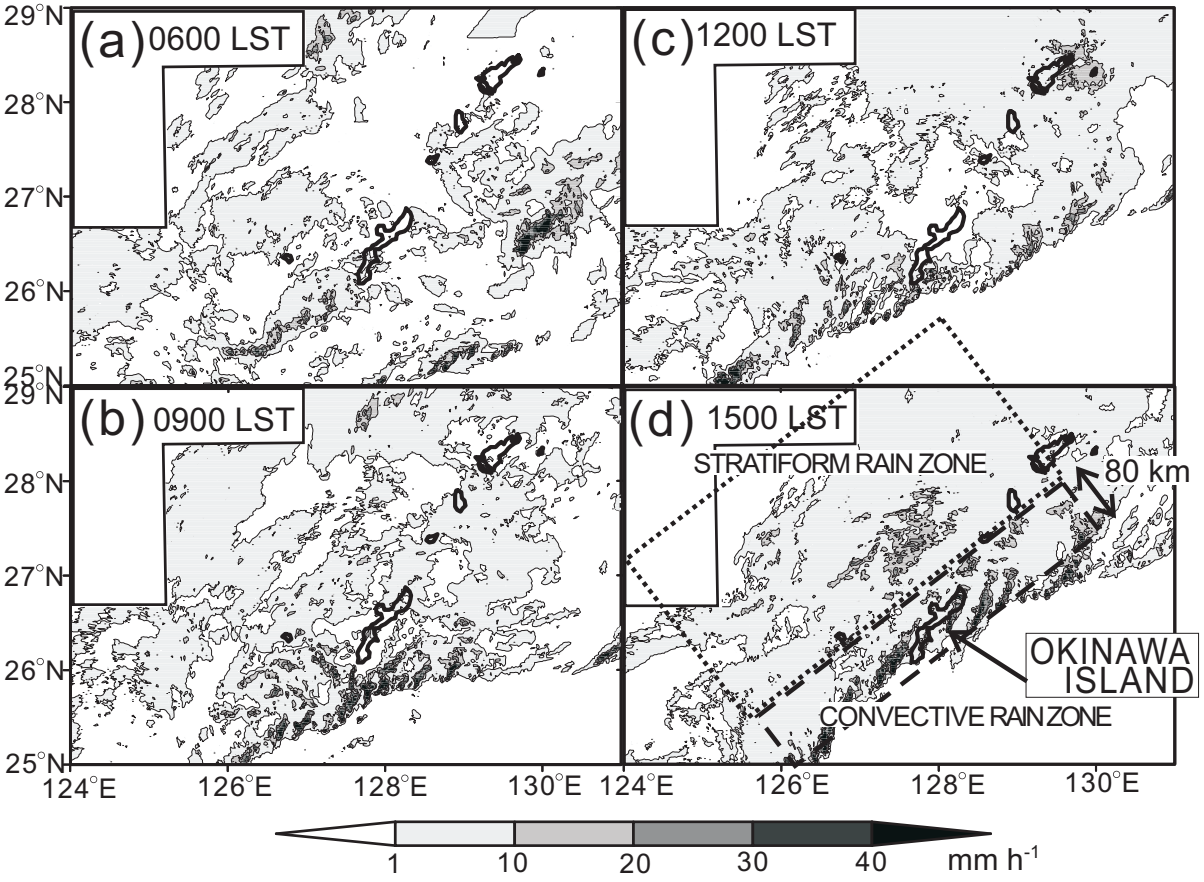

Fig. 5. Horizontal distributions of hourly rain intensity at 2 km ASL, estimated by JMA operational radar at (a) 0600 LST, (b) 0900 LST, (c) 1200 LST, and (d) 1500 LST on 10 June 2006. Regions bounded by a dotted line in (d) and a dashed line in (d) denote a stratiform rain zone and a convective rain zone, respectively.

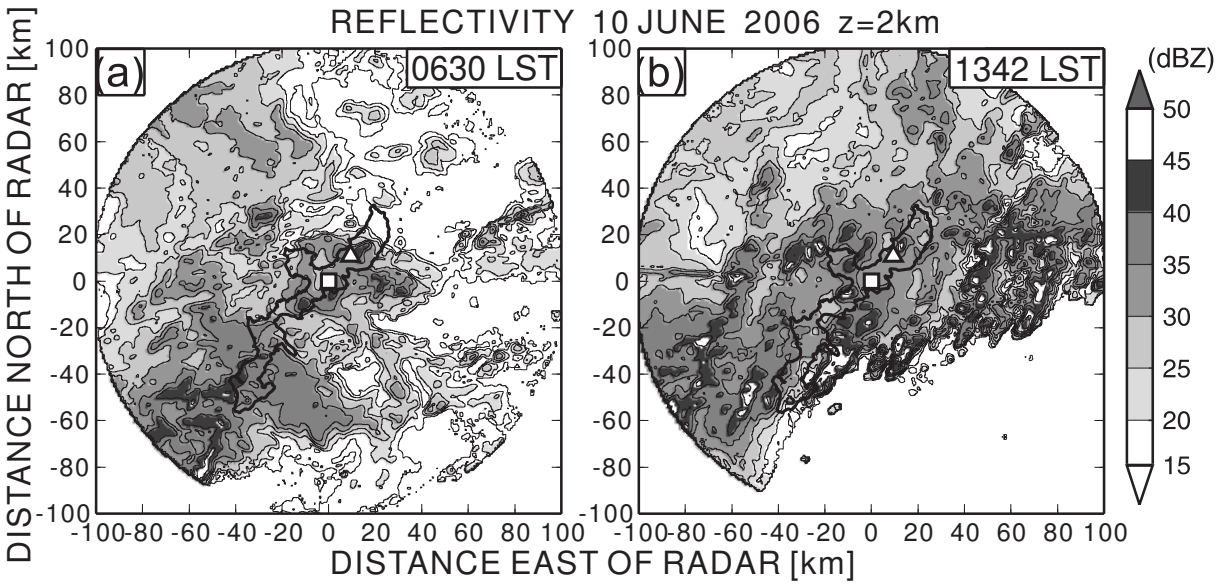

Fig. 6. Horizontal distributions of Z_{h} at 2 km ASL (CAPPI) at (a) 0630 LST and (b) 1342 LST. The open square and open triangle denote the radar and disdrometer locations, respectively.

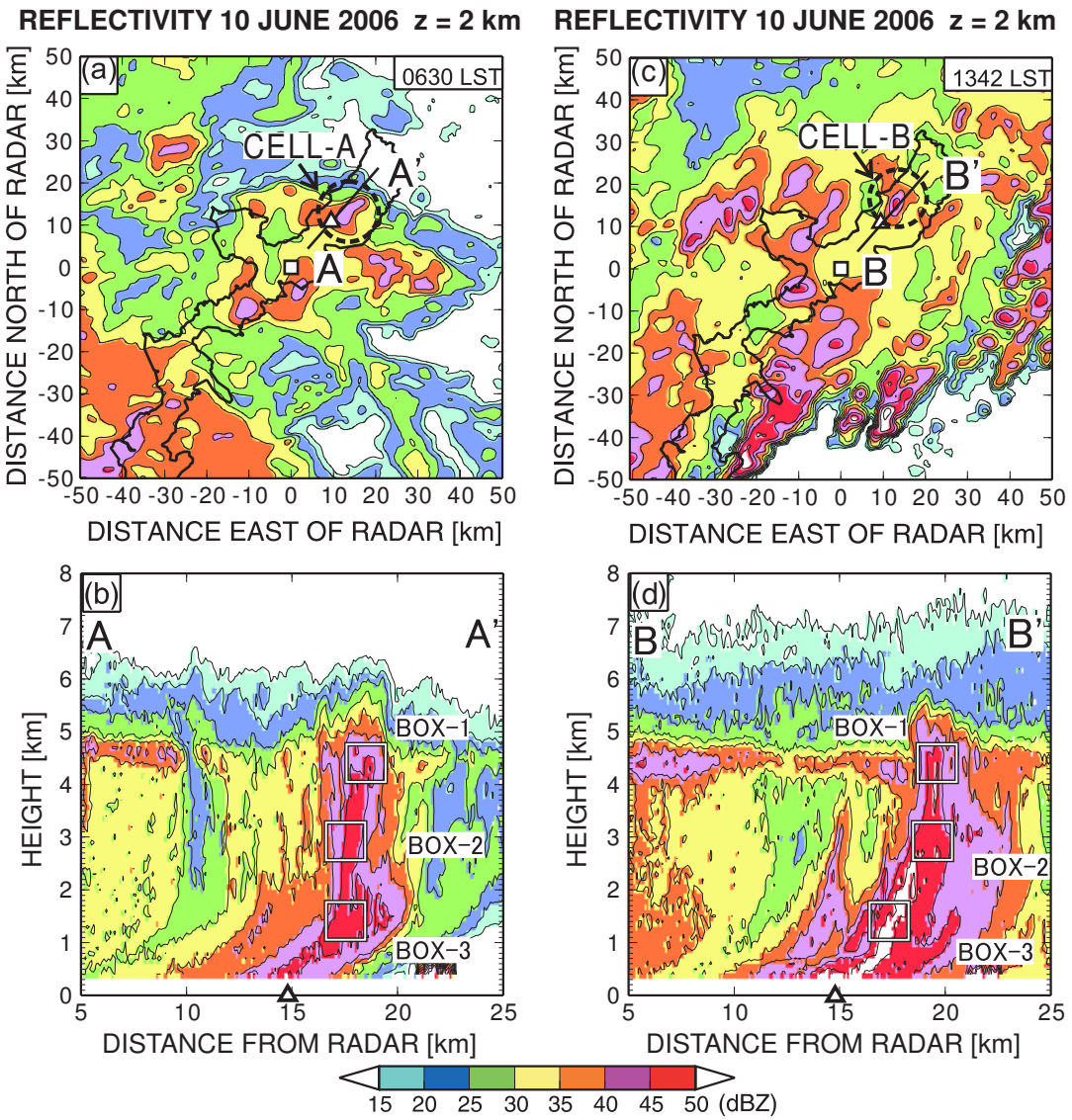

Fig. 7. CAPPIs showing horizontal cross sections of $Z_{\rm h}$ at (a) 0630 LST and (c) 1342 LST at 2 km ASL. Vertical cross sections (RHI) of $Z_{\rm h}$ at (b) 0630 LST and (d) 1342 LST along A-A$'$ in (a) and along B-B$'$ in (c), respectively. CELL-A and CELL-B are bounded by dashed lines in (a) and (c), respectively, and indicated by arrows in (a) and (c), respectively. Rectangles in (b) and (d) present the analysis areas of $Z_{\rm DR}$ and $\rho_{\rm hv}$. Each area is 2 km in the horizontal and 0.8 km (4.0−4.8 km for BOX-1, 2.5−3.3 km for BOX-2, and 1.0−1.8 km for BOX-3) in the vertical. The open square and open triangle denote the radar and disdrometer locations, respectively.

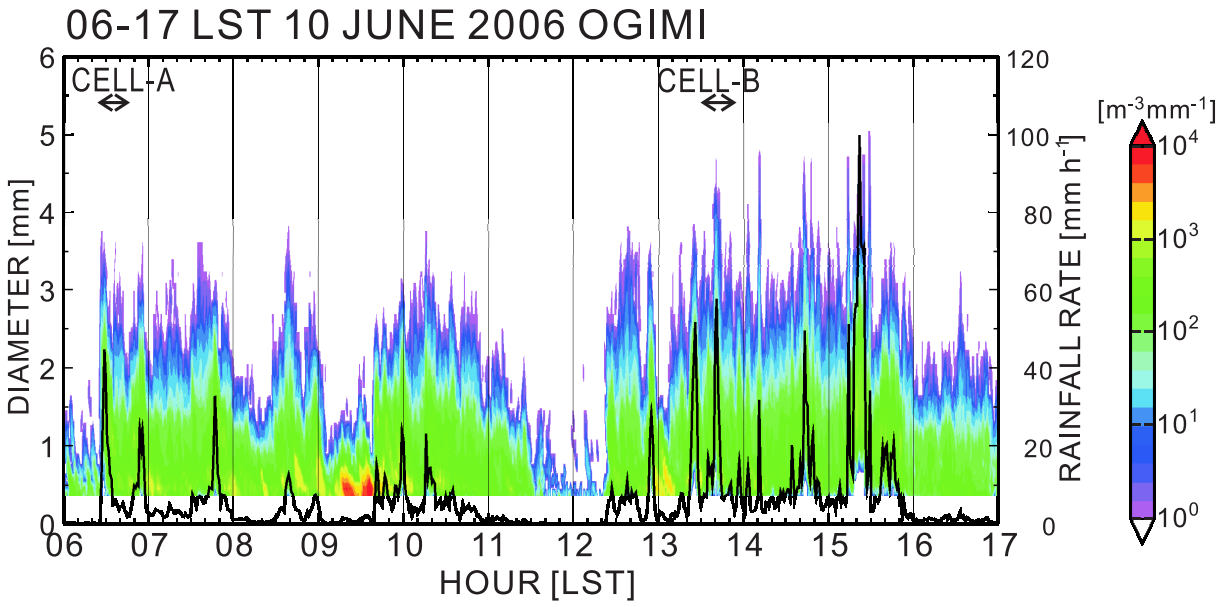

Fig. 8. Time series of 1-min integrated DSD (shade) and 1-min averaged rainfall intensity (solid line) measured by the disdrometer at Ogimi on 10 June 2006. Color shade indicates the number of raindrops per the cubic meter in the unit diameter (1 mm). Periods of the passages of CELL-A and CELL-B are indicated by two-headed arrows.

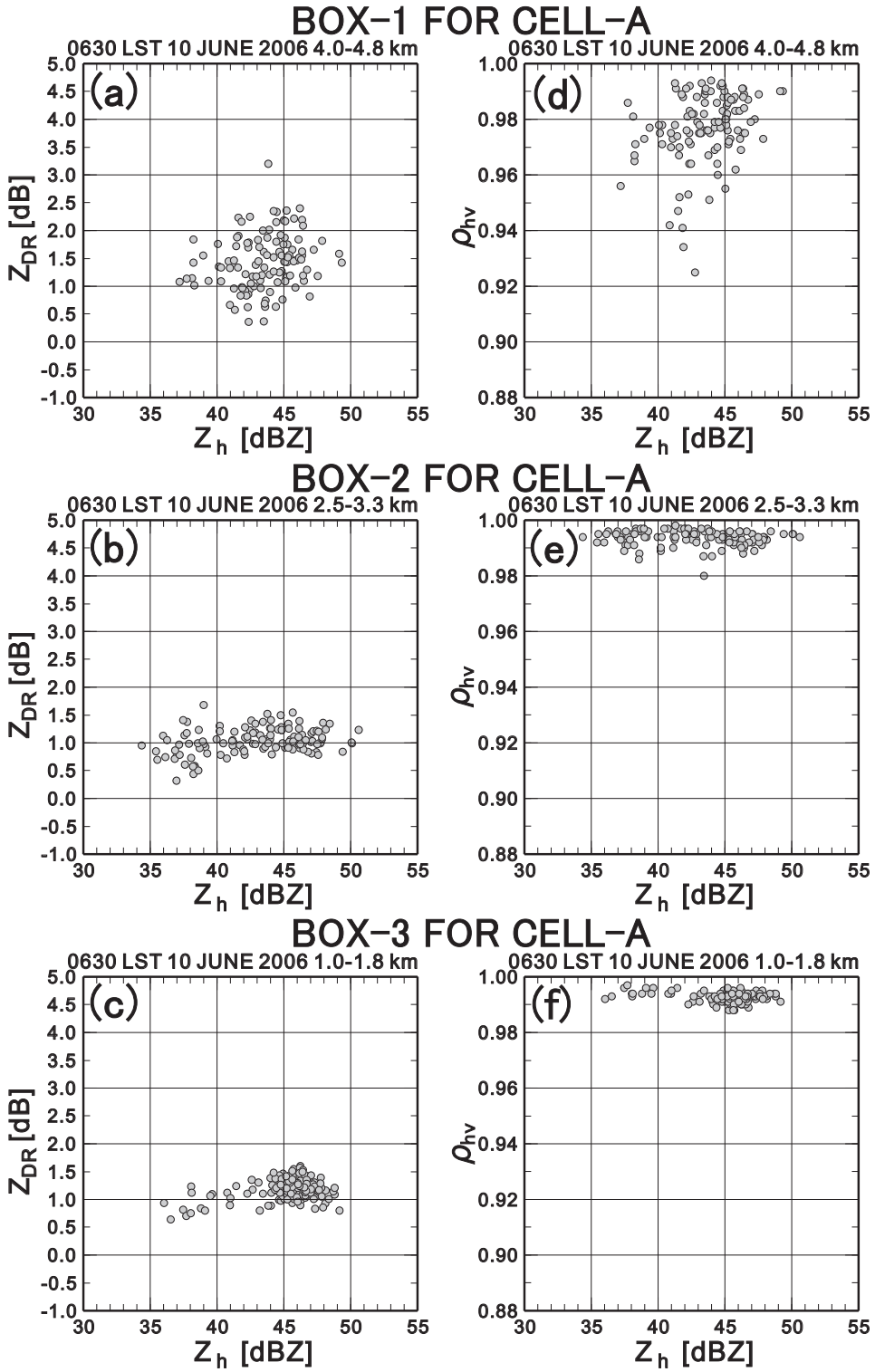

Fig. 9. Scattering diagrams of Z_{h} versus Z_{DR} for CELL-A within (a) BOX-1, (b) BOX-2, and (c) BOX-3 in Fig. 7b and Z_{h} versus ρ_{hv} for CELL-A within (d) BOX-1, (e) BOX-2, and (f) BOX-3 in Fig. 7b. The plotted data are RHI range bin data at 0630 LST.

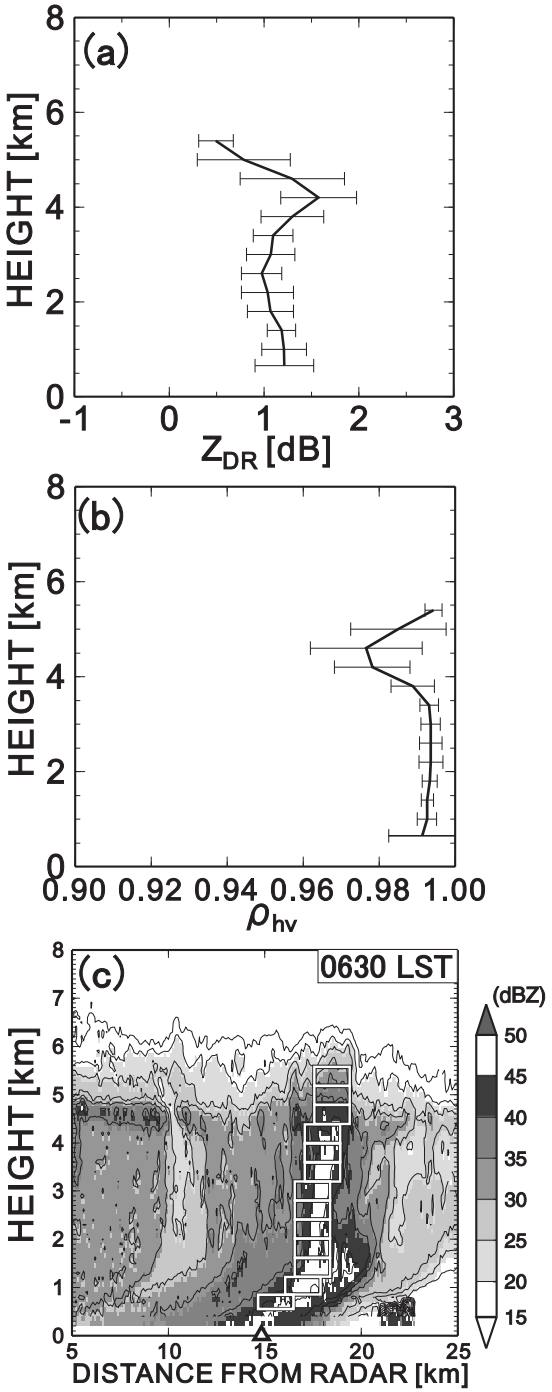

Fig. 10. Vertical profiles of (a) averaged Z_{DR} and (b) averaged ρ_{hv} of CELL-A. Error bars in (a) and (b) are standard deviations. These averages were calculated from RHI range bin data of the areas presented by rectangles in (c) representing the vertical cross section (RHI) of radar reflectivity at 0630 LST. Each area in (c) is 2 km in the horizontal and 0.4 km in the vertical in the RHI, except for the lowest box which is 0.3 km in the vertical. The open triangle in (c) denotes the disdrometer location.

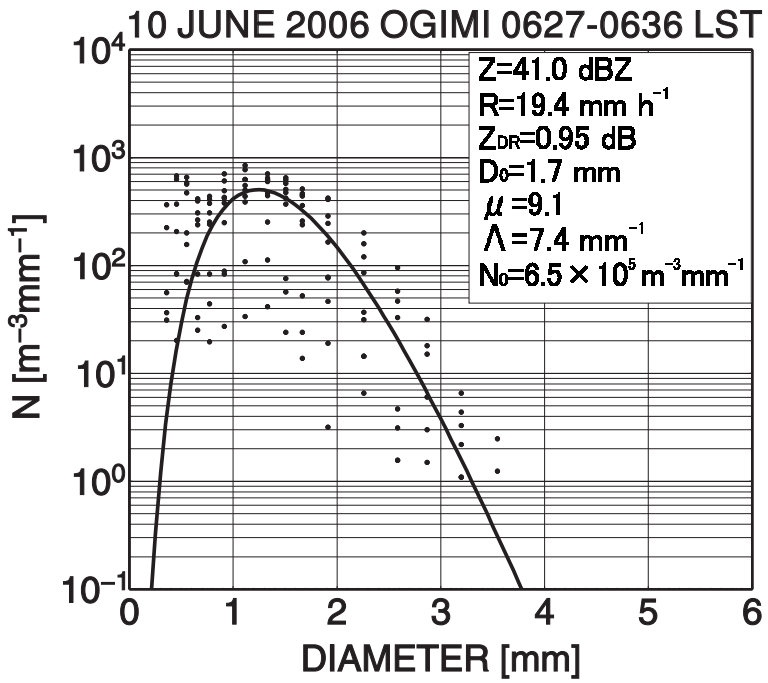

Fig. 11. The ground-based DSD measured by the disdrometer at Ogimi during the passage of CELL-A (from 0627 to 0636 LST). The dots show 1-min DSDs, and the solid curve shows a gamma function calculated from the temporally integrated DSD during the passage of a cell. Variables give the radar reflectivity factor (Z) derived from the integrated DSD, rainfall intensity (R) derived from the integrated DSD, and parameters of the gamma function (μ: shape parameter, Λ: slope parameter, and N_0: intercept parameter).

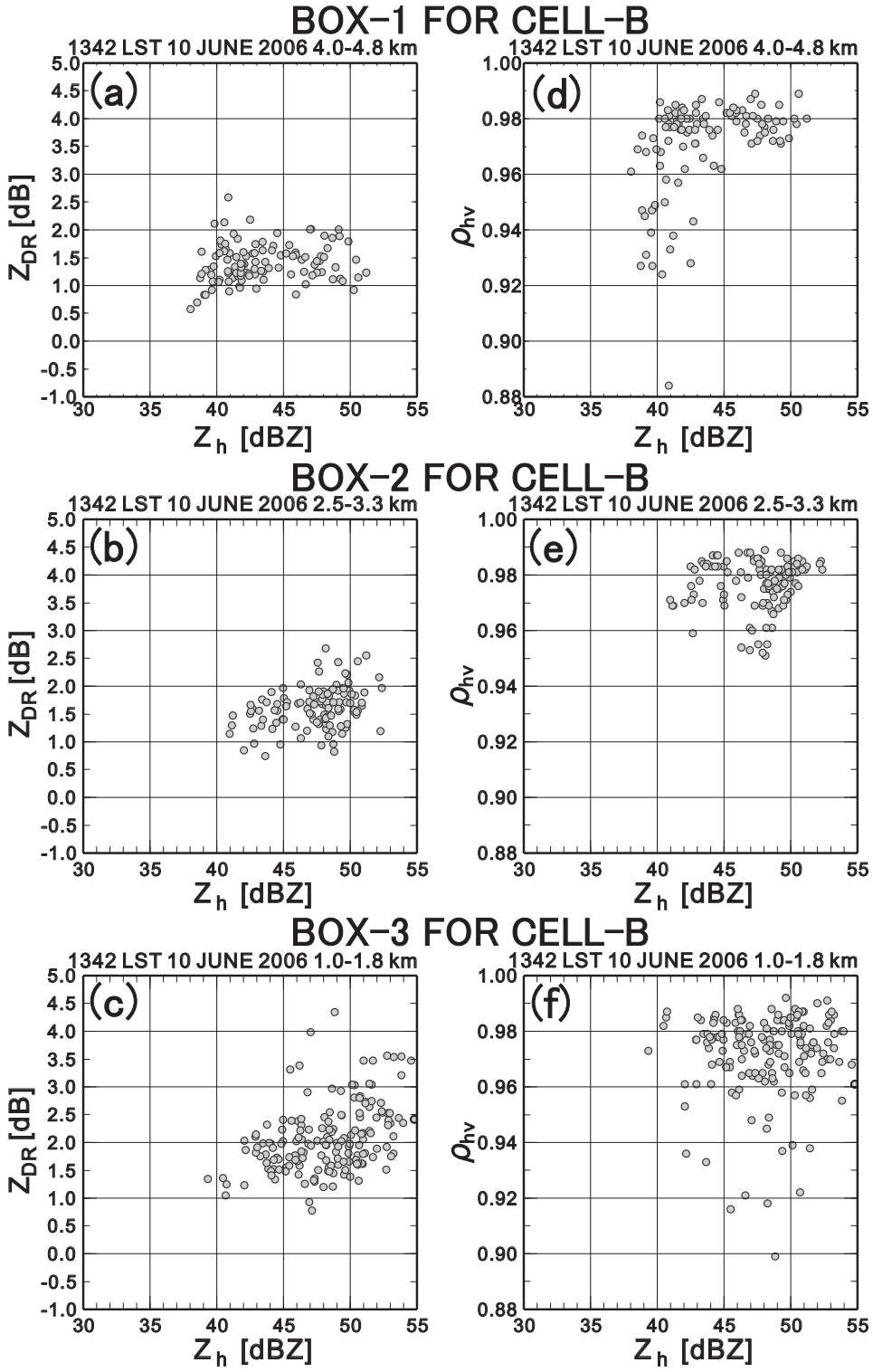

Fig. 12. As in Fig. 9, but for CELL-B at 1342 LST.

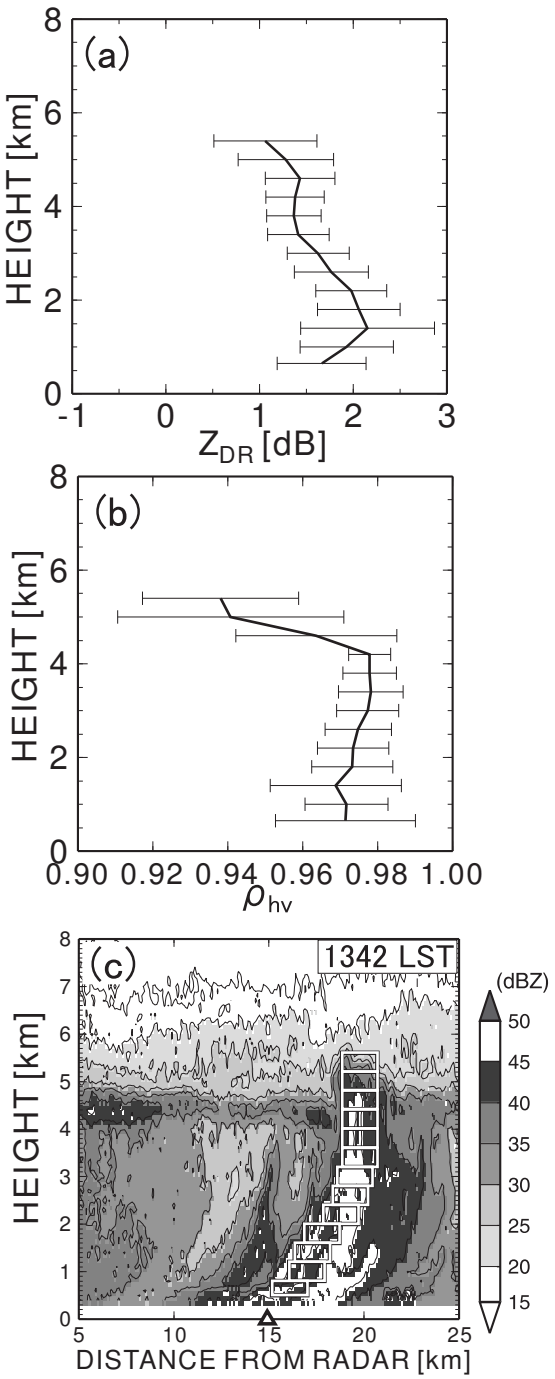

Fig. 13. As in Fig. 10, but for CELL-B at 1342 LST.

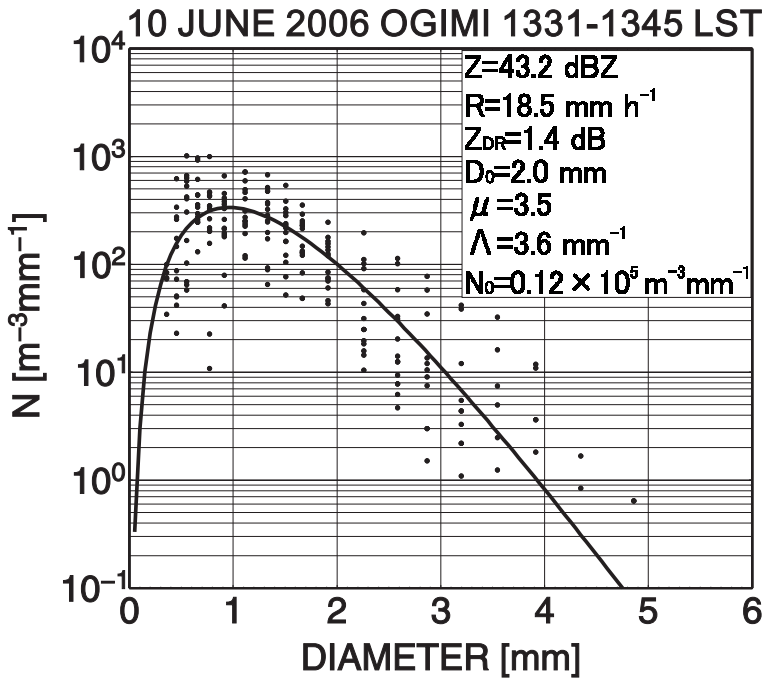

Fig. 14. As in Fig. 11, but for CELL-B (from 1331 to 1345 LST).

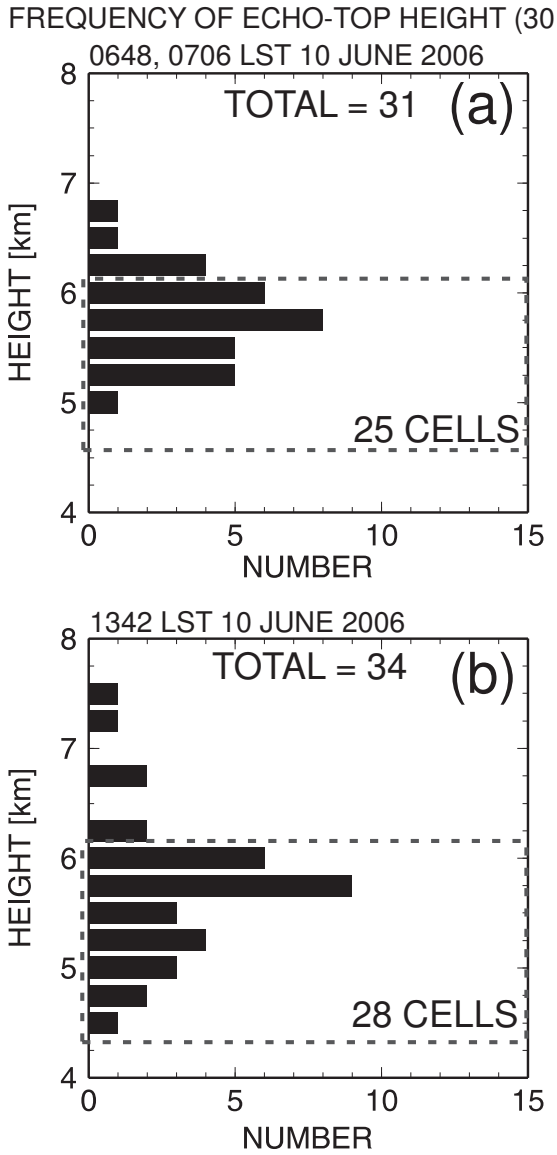

Fig. 15. Frequency of the echo-top height (of 30 dBZ) of convective cells found (a) in the stratiform rain zone in CAPPIs at 0648 and 0706 LST and (b) in the convective rain zone in the CAPPI at 1342 LST. The radar's sampling range (r) of convective cells was 10 km $\leq$ r $\leq$ 50 km. The 25 cells of 31 total cells in (a) and the 28 cells of 34 total cells in (b) having echo-top heights less than 6.0 km ASL were selected for analyses.

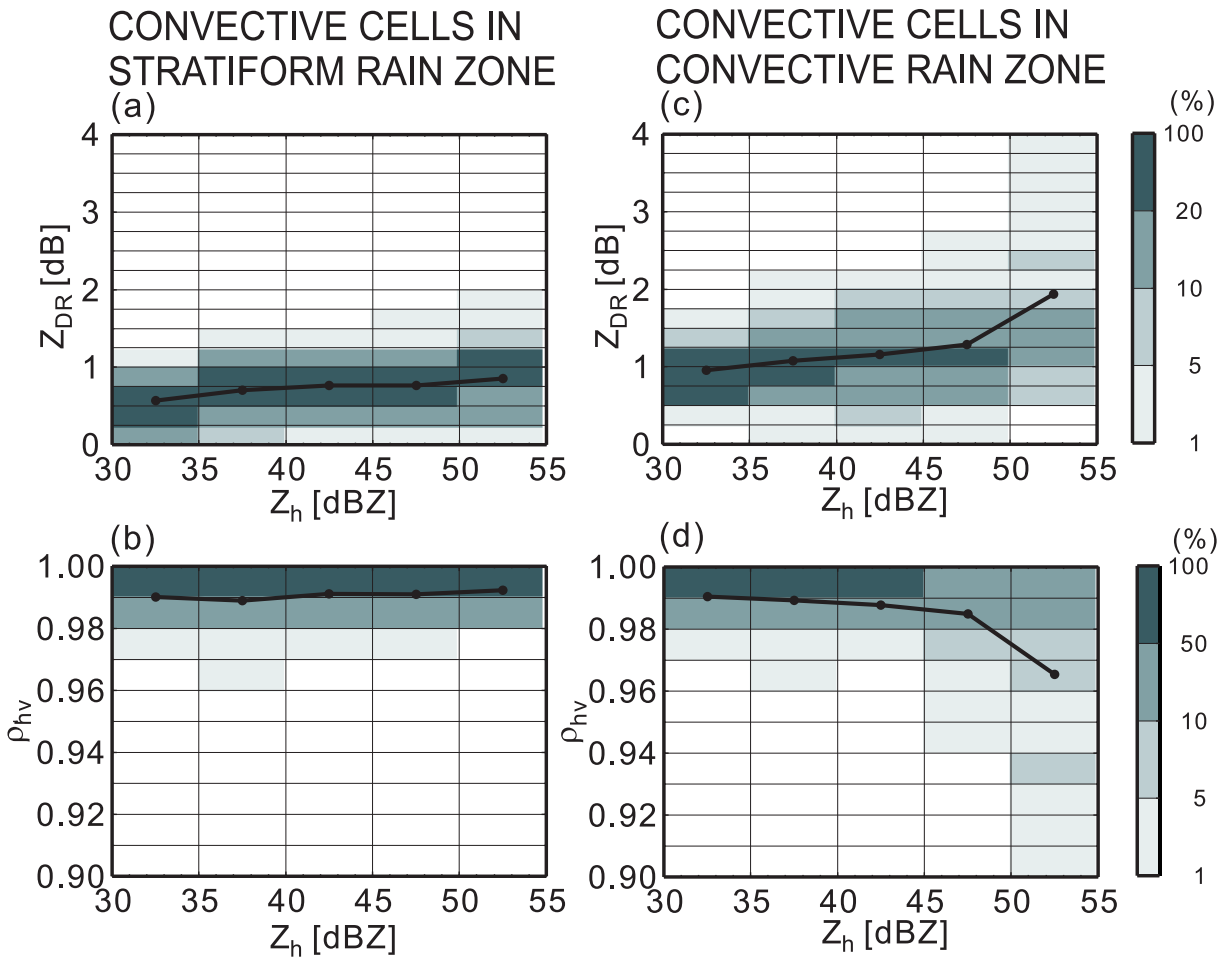

Fig. 16. Diagrams of mean by 5-dB reflectivity (solid lines) and frequency by 5-dB reflectivity (shading) of (a) $Z_{\rm DR}$ and (b) $\rho_{\rm hv}$ in PPIs between 0.7 km and 3.0 km ASL with 30 dB$Z \leq Z_{\rm h} < 55$ dBZ for 25 convective cells existing in the stratiform rain zone presented in Fig. 15a, except for convective cells with echo-top height above 6.0 km. The PPI data shown were corrected from 2 km × 2 km horizontal columns centered around cores for each convective cell every 1.0 km altitude in CAPPIs. Panels (c) and (d) are the same as (a) and (b), respectively, but for 28 convective cells existing in the convective rain zone presented in Fig. 15b.

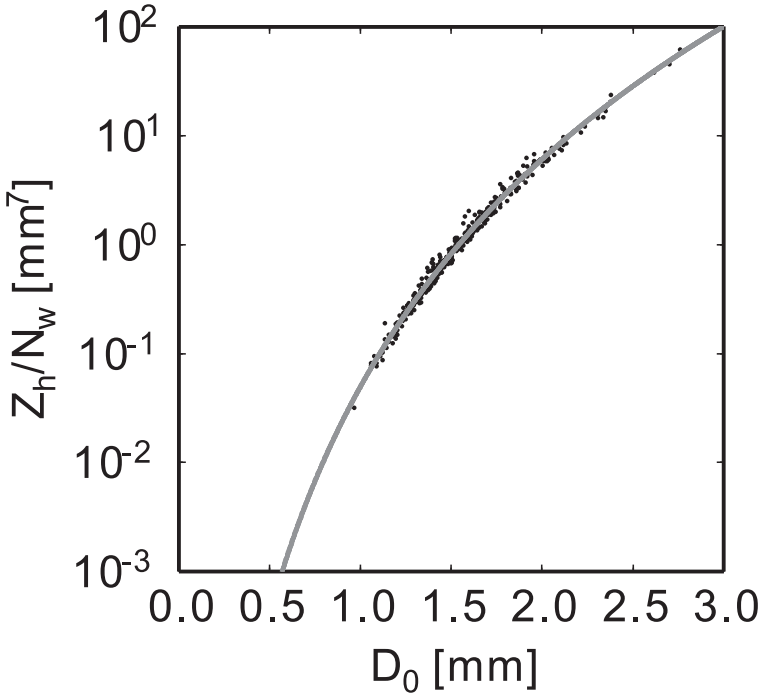

Fig. 17. Scattering diagram of D_0 versus '$Z_{\rm h}/N_w$' with best fit curve derived from ground-based DSD. The ground-based DSD data used for estimating the best fit were acquired during precipitation with rainfall rate greater than 3 mm h^{-1}

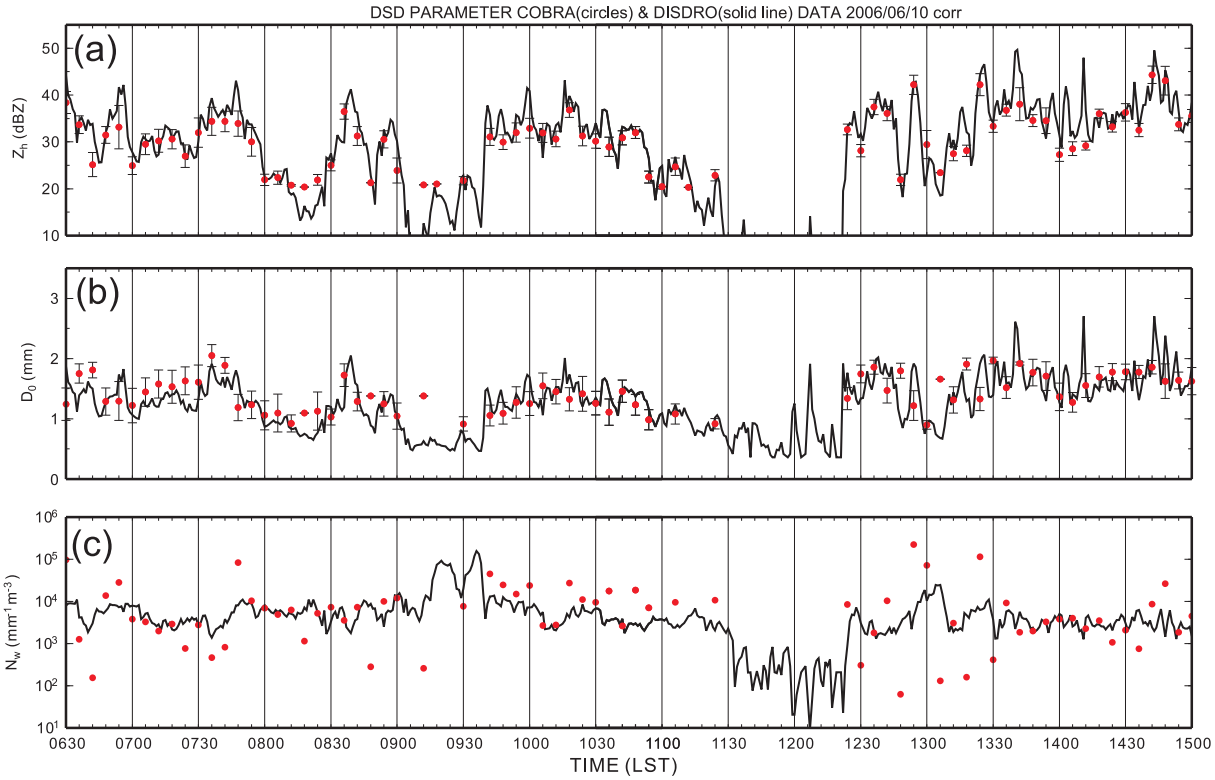

Fig. 18. Time series of (a) $Z_{\rm h}$, (b) D_0, and (c) N_w comparing the disdrometer measurements (solid line) and radar estimates (closed circles) during precipitation from 0630 LST to 1500 LST on 10 June 2006. The radar-estimated variables were areally averaged over a 1-km horizontal area centered around the location of the disdrometer, using data from the PPI scans of 1.1 degrees. The error bars shown in (a) and (b) represent standard deviations.

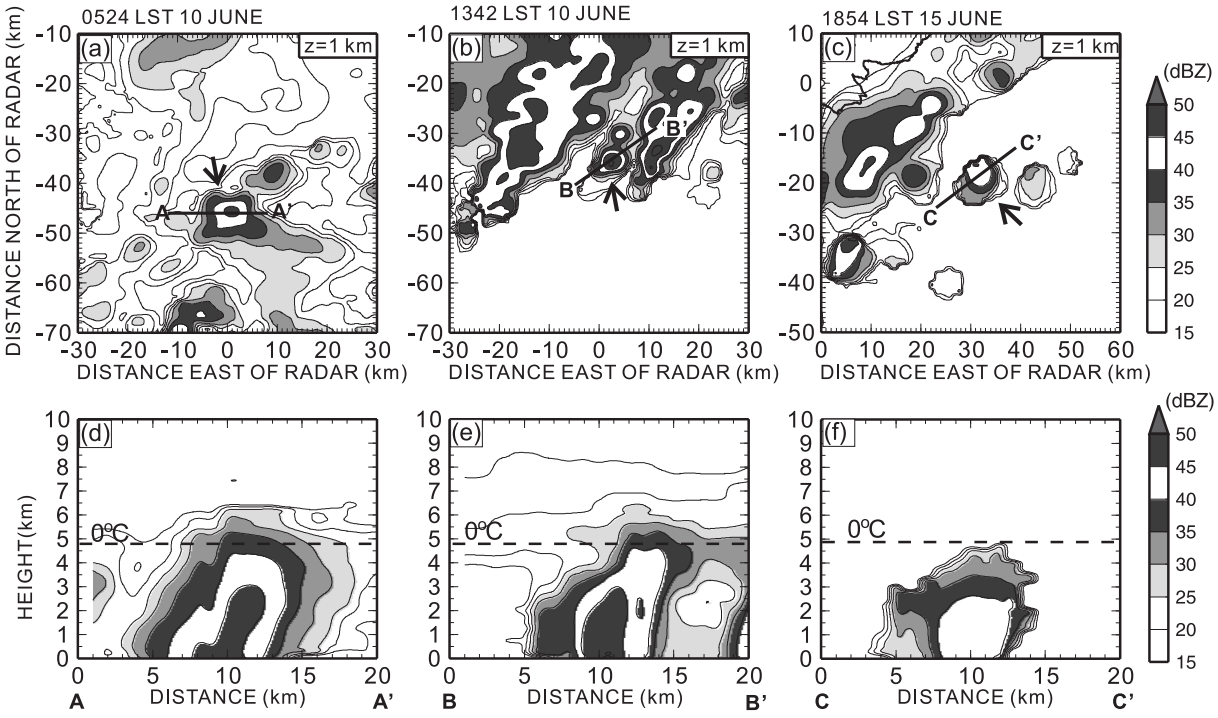

Fig. 19. Horizontal distributions of Z_{h} in CAPPIs at 1 km ASL for (a) the convective cell in the stratiform rain zone at 0524 LST on 10 June, (b) the convective cell in the convective rain zone at 1342 LST on 10 June, and (c) the isolated convective cell at 1854 LST on 15 June in their mature stages. The convective cells are indicated by arrows in each figure. (d,e,f) Vertical cross sections along lines shown in (a), (b), and (c), respectively. Dashed lines indicate the 0°C altitude.

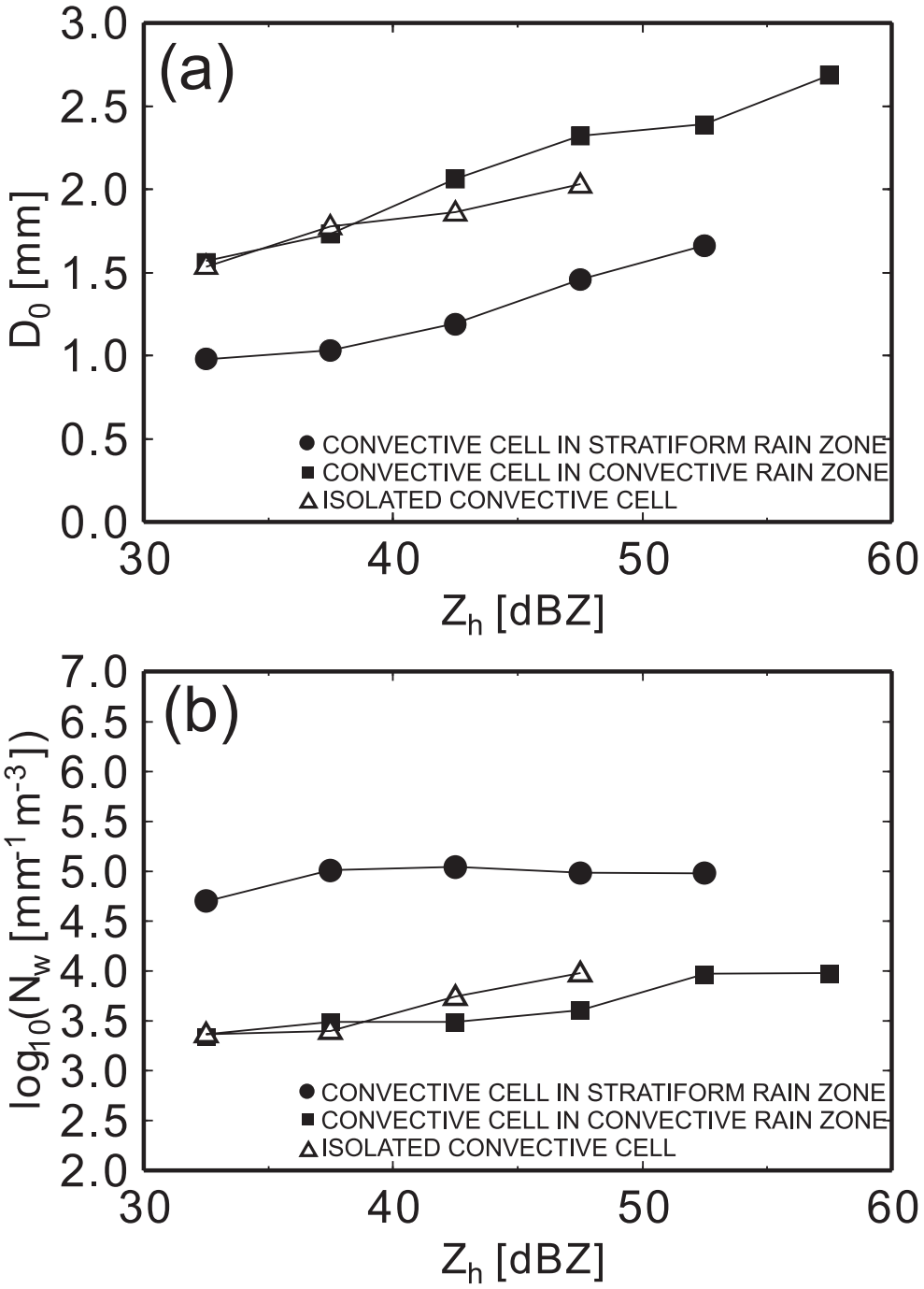

Fig. 20. (a) Radar-estimated D_0 versus $Z_{\rm h}$ and (b) radar-estimated N_w versus $Z_{\rm h}$ for convective cells in their mature stages. The estimated values shown in this figure are D_0 averaged per 5 dB in $Z_{\rm h}$ and the logarithmic average of N_w per 5 dB in $Z_{\rm h}$. The dots correspond to points of the convective cell in the stratiform rain zone (0524 LST on 10 June), the squares denote the convective cell in the convective rain zone (1342 LST on 10 June), and the triangles represent the isolated convective cell (1854 LST on 15 June). The mean values were calculated from PPI scanning data obtained between 0.5 km and 3.0 km ASL for each convective cell.

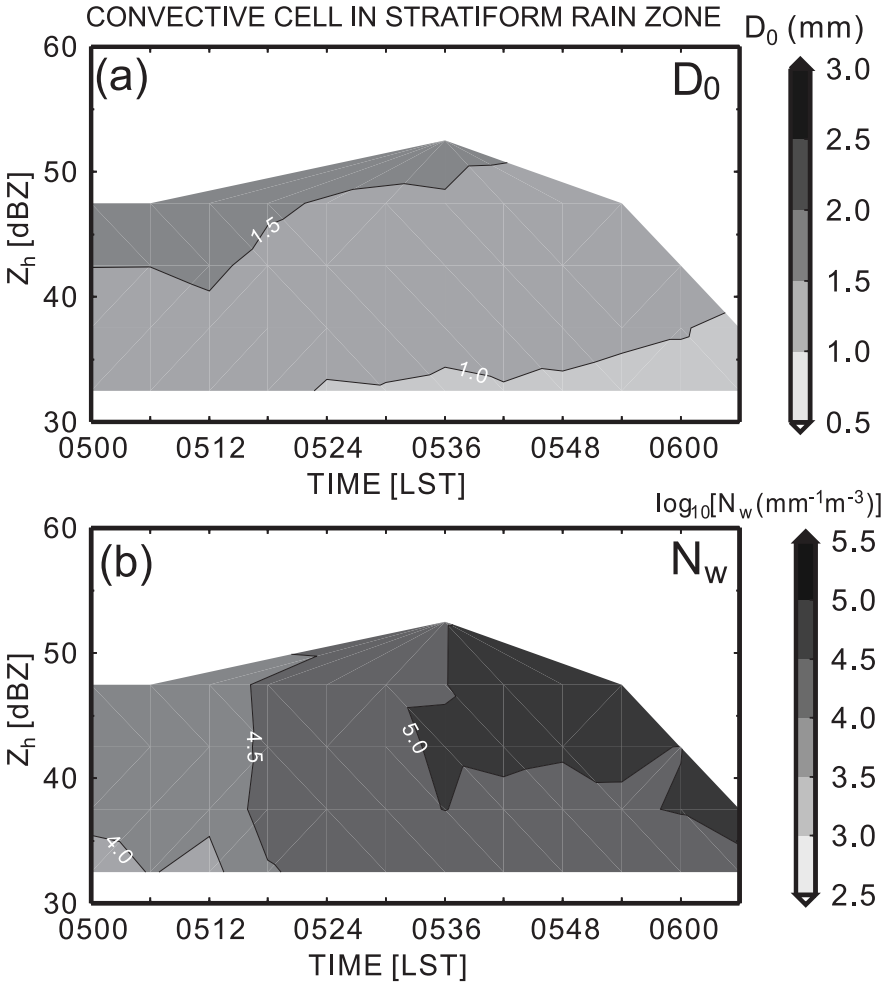

Fig. 21. Z_{h}-time sections of (a) the radar-estimated D_0 and (b) the radar-estimated N_w for the convective cell in the stratiform rain zone from 0500 LST to 0606 LST on 10 June. The estimated values shown in this figure are D_0 averaged per 5 dB in Z_{h} and the logarithmic average of N_w per 5 dB in Z_{h}, using PPI scanning data obtained between 0.5 km and 3.0 km ASL for each PPI volume scan.

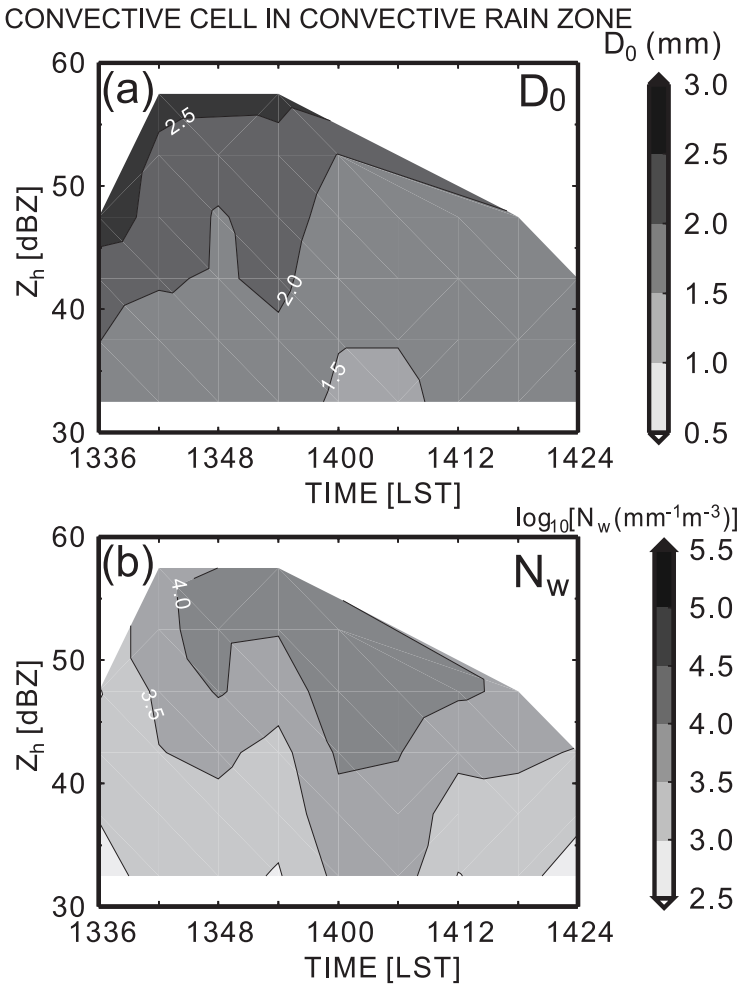

Fig. 22. As in Fig. 21, but for the convective cell in the convective rain zone from 1336 LST to 1424 LST on 10 June.

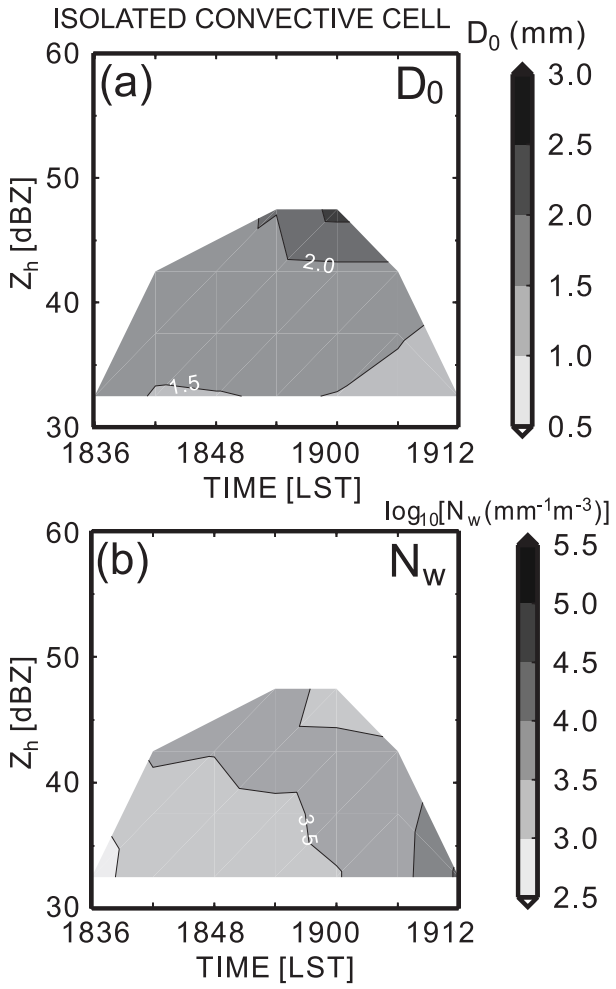

Fig. 23. As in Fig. 21, but for the isolated convective cell from 1836 LST to 1912 LST on 15 June.

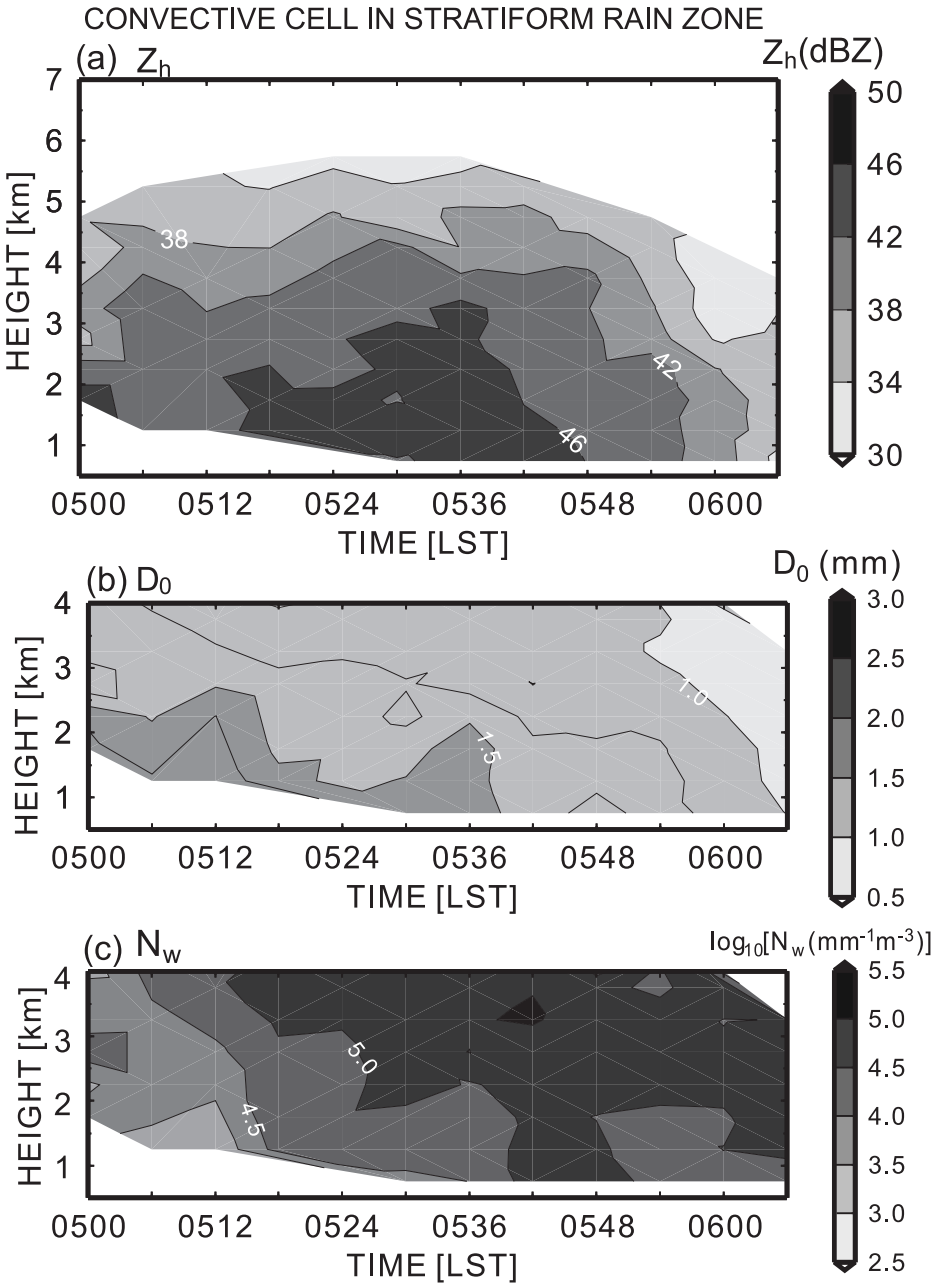

Fig. 24. Height-time sections of the (a) radar-measured $Z_{\rm h}$, (b) radar-estimated D_0, and (c) radar-estimated $\log_{10}N_w$ for the convective cell in the stratiform rain zone from 0500 LST to 0606 LST on 10 June. The values were averaged every 5-km of altitude, using PPI data collected from 2 km × 2-km horizontal and 0.25-km vertical boxes centered around cores for each convective cell every 0.25 km altitude in CAPPIs. The N_w were logarithmically averaged. The contours in (b) indicate D_0 every 0.25 mm.

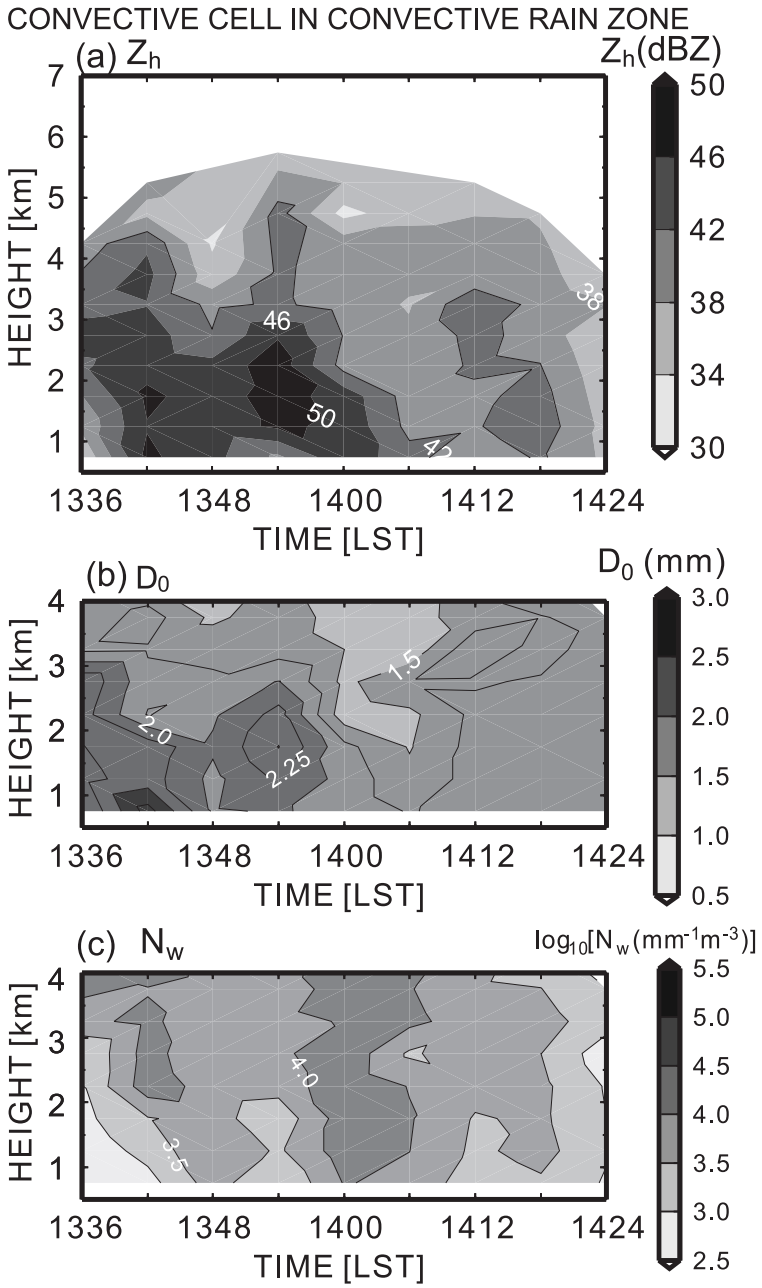

Fig. 25. As in Fig. 24, but for the convective cell in the convective rain zone from 1336 LST to 1424 LST on 10 June.

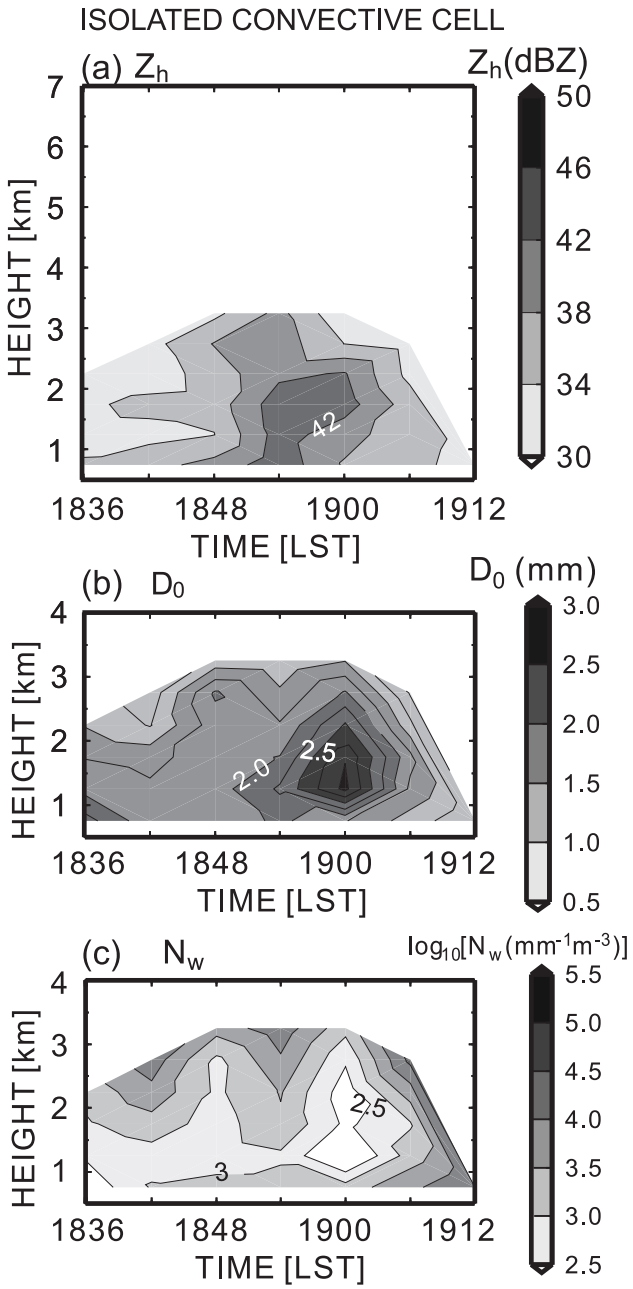

Fig. 26. As in Fig. 24, but for the isolated convective cell from 1836 LST to 1912 LST on 15 June.

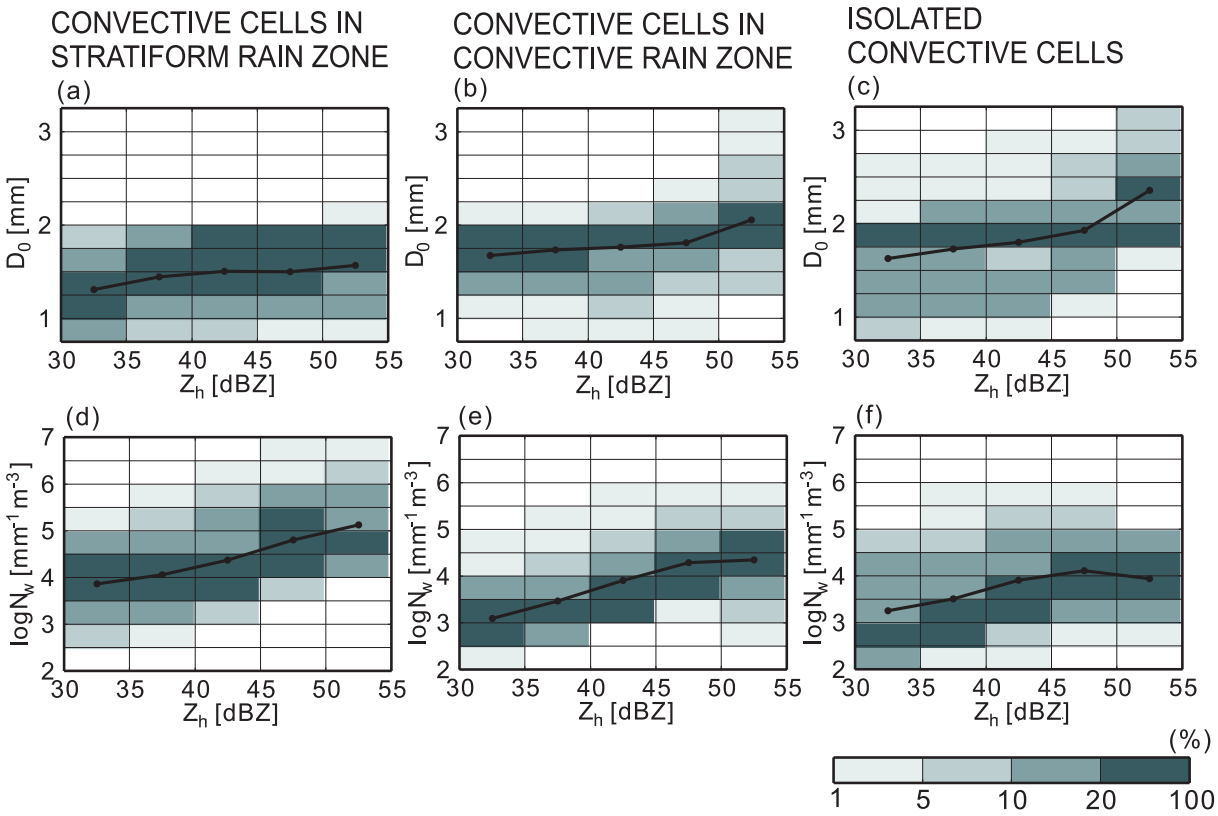

Fig. 27. Diagrams of mean by 5-dB reflectivity (solid lines) and frequency by 5-dB reflectivity (shading) of radar-estimated D_0 (a) for 25 convective cells in the stratiform rain zone, (b) for 28 convective cells in the convective rain zone, and (c) for 14 isolated convective cells. The D_0 values estimated from range bin data in PPIs between 0.7 km and 3.0 km ASL with 30 dB$Z \leq Z_{\rm h} < 55$ dBZ. The PPI data shown were corrected from 2 km $\times$ 2 km horizontal columns centered around cores for each convective cell every 1.0 km altitude in CAPPIs. Selected 25 convective cells in the stratiform rain zone and 28 convective cells in the convective rain zone were the same as those for Fig. 16. 14 isolated convective cells, which had 30-dBZ echo-top heights less than 6 km ASL, were selected from CAPPIs at 1554, 1624, 1654, 1848, and 1900 LST. Panels (d), (e), and (f) are the same as (a), (b), and (c), respectively, but for $\log_{10} N_w$. The N_w values were logarithmically averaged.

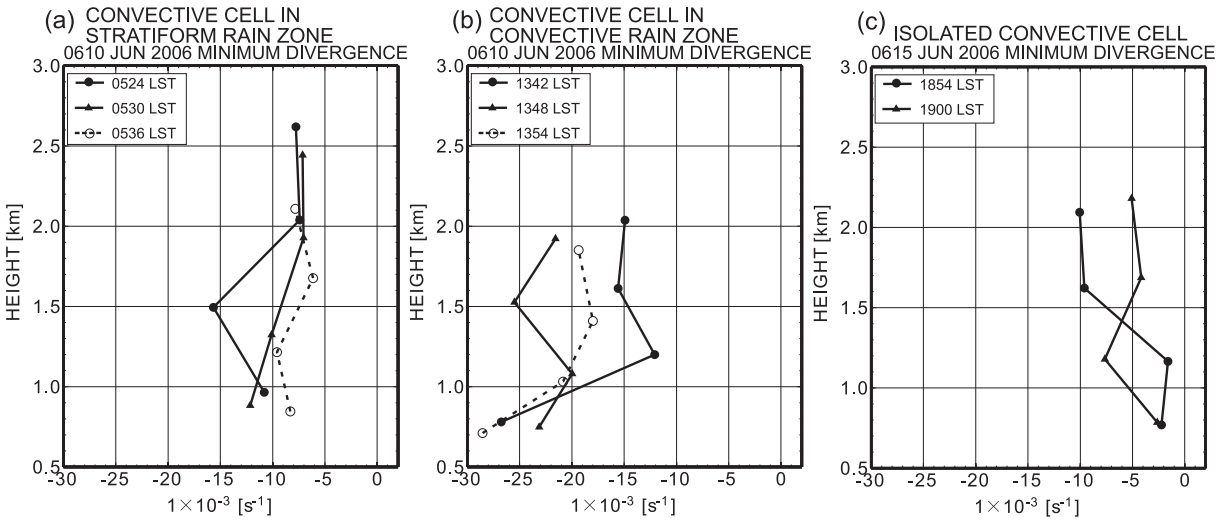

Fig. 28. Minimum divergence, which means maximum convergence, estimated from Doppler velocity in PPIs for (a) the convective cell in the stratiform rain zone, (b) the convective cell in the convective rain zone, and (c) the isolated convective cell. Each value was estimated from range bin data in a PPI in convective cell area.

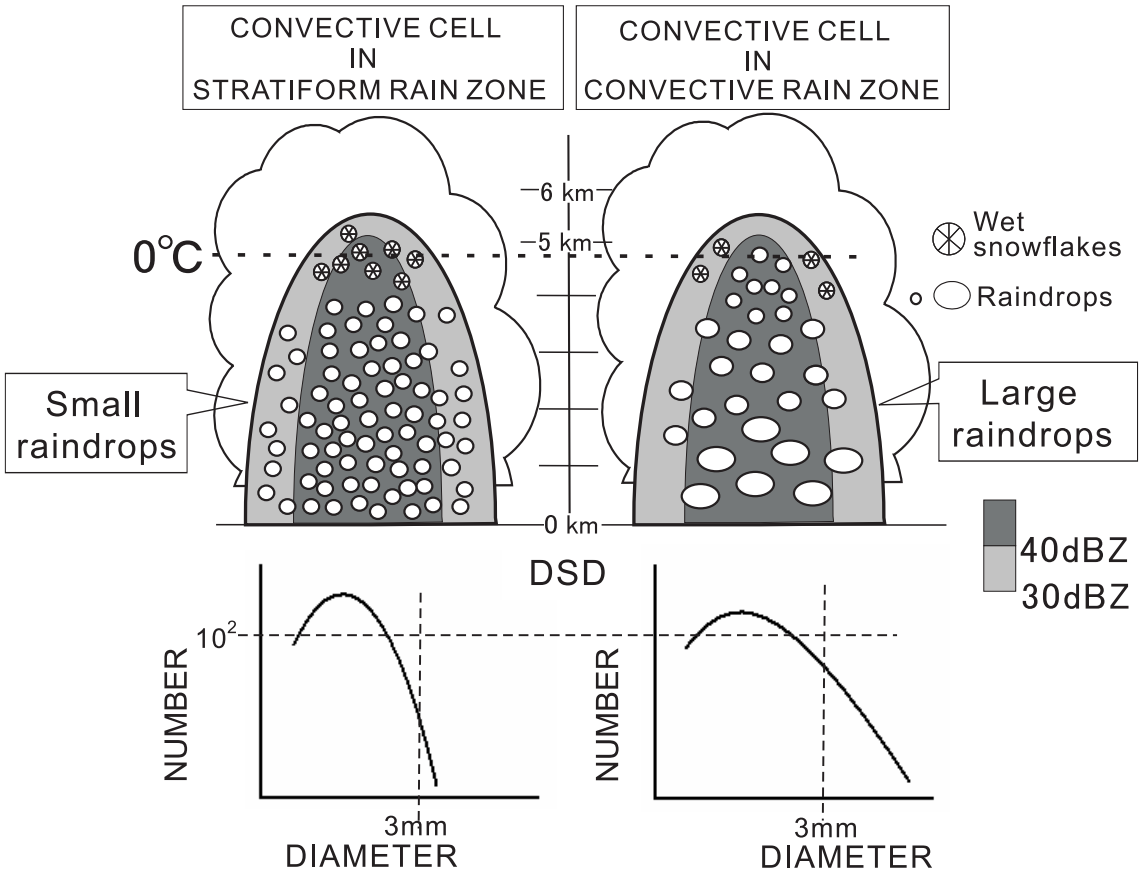

Fig. 29. Conceptual diagram of precipitation-particle distributions in a convective cell in a stratiform rain zone (left) and in a convective cell in a convective rain zone (right). The gray scale shows the radar reflectivity. Corresponding ground-measured DSDs are shown at the bottom of the figure.

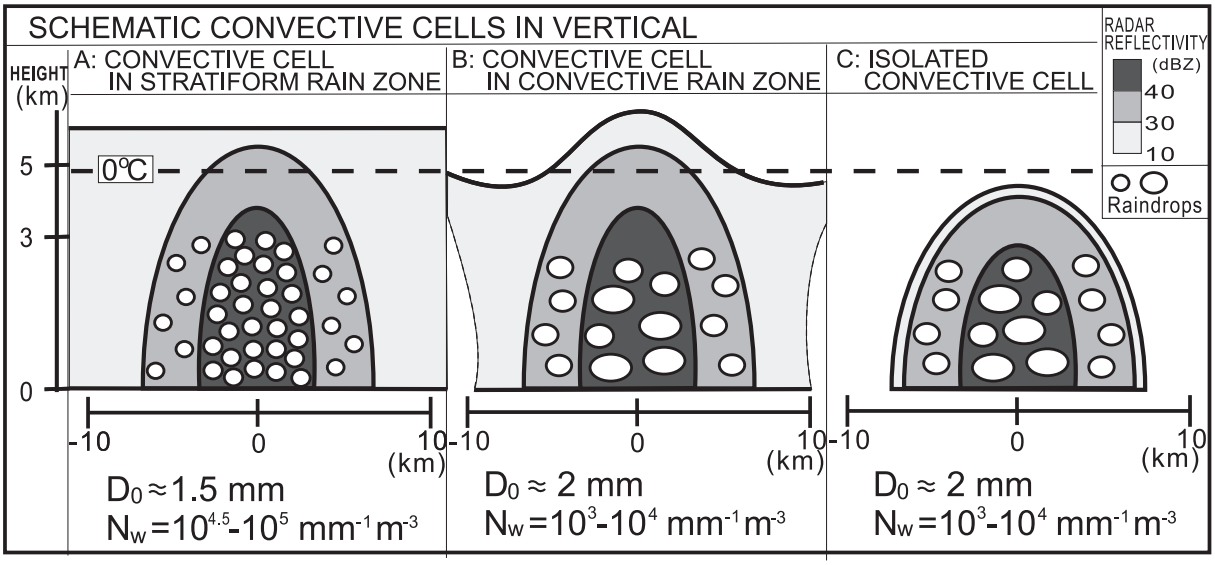

Fig. 30. Schematic convective cells with DSD characteristics considered from DSD parameters estimated from polarimetric radar measurements. (Left) Convective cell in stratiform rain zone. (Middle) Convective cell in convective rain zone. (Right) Isolated convective cell. Shading represents the radar reflectivity, Z_{h}. Dashed line represents the 0°C altitude. Values of the estimated DSD parameters indicate mean values in the mature stage of the convective cells. Note that D_0 values in this figure are mean values with Z_{h} around 45 dBZ.